Spring 5-2024

Modeling of Rotor Wake Vortex Dynamics and Interactions in Non-Homogenous Vertiport Environments

Garrison P. Shaw
Embry-Riddle Aeronautical University, shawg@my.erau.edu

MODELING OF ROTOR WAKE VORTEX DYNAMICS AND INTERACTIONS IN NON-HOMOGENOUS VERTIPORT ENVIRONMENTS.

By

Garrison P. Shaw

A Thesis Submitted to the Faculty of Embry-Riddle Aeronautical University

In Partial Fulfillment of the Requirements for the Degree of

Master of Science in Aerospace Engineering

May 2024

Embry-Riddle Aeronautical University

Daytona Beach, Florida

MODELING OF ROTOR WAKE VORTEX DYNAMICS AND INTERACTIONS IN NON-HOMOGENOUS VERTIPORT ENVIRONMENTS.

By

Garrison Shaw

This Thesis was prepared under the direction of the candidate's Thesis Committee Chair, Dr. [Jill Smith], Department of Aerospace Engineering, and has been approved by the members of the Thesis Committee. It was submitted to the Office of the Senior Vice President for Academic Affairs and Provost, and was accepted in the partial fulfillment of the requirements for the Degree of Master of Science in Aerospace Engineering.

THESIS COMMITTEE

Chair, Dr. Vladimir Golubev	Member, Dr. Tasos Lyrinitzis
Member, Dr. Reda Mankbadi	
Graduate Program Coordinator, Dr. Hever Moncayo	Date
Dean of the College of Engineering, Dr. James W. Gregory	Date
Associate Provost of Academic Support, Dr. Kelley Austin	Date

To my Lord and savior Jesus Christ, Whom I couldn't take a breath without His gracious hand.

ACKNOWLEDGEMENTS

I would like to thank my Advisor Dr. Vladimir Golubev and my committee members Dr. Reda Mankbadi, Dr. Tasos Lyrintzis. for assisting me with my work and giving me valuable insight. I would like to thank Micheal Goncalves for providing immeasurable help in the development of this work, and Dr. Pamela Daniels for providing fantastic input in the final stretch. I would also like to thank Embry-Riddle Aeronautical University for allowing me the opportunity to use their facilities and I would like to thank National Aeronautical Space Administration (NASA) University Leadership Initiative (ULI) for sponsoring this project and allowing me access the High-End Computational Cluster (HECC) supercomputer. My deepest gratitude goes to my friends and family who have been there through the entire process providing support when I needed it.

ABSTRACT

The current research serves to analyze and study the effects ground forces can have on the thrust performance of a propeller in multiple different configurations. The current research utilizes an open source Computational Fluid Dynamics (CFD) software known as OpenFOAM to generate calculate and visualize these runs. The model used for this experiment is a hybrid model that employs both a Unsteady Reynolds-Averaged Navier-Stokes (URANS) and a detached eddy simulation using a hybrid Large Eddy Simulation (LES) via a KomegaSSTDDES model. This model serves to save computational time as well as allow for accurate results. The three cases run are isolated rotor, full ground effects and partial ground effects. It was discovered that the full ground effects and the partial ground effects caused the thrust to trend slightly up. Even with this discovery it is reasonable to assume that due to the distance in which the rotor was placed that the change in overall thrust will be minimal however the effects caused by the way the wake develops can cause significant challenges in implementing electric vertical takes off and landing devices (EVTOL's) in modern urban environments. Acoustic data was also observed in this sphere with the main goal being to observe the impact the ground has on the noise. These results showed a trend similar to the performance data with only a slight increase in the noise recorded.

TABLE OF CONTENTS

ACKNOWLEDGEMENTS……iii

ABSTRACT……iv

LIST OF FIGURES……vii

LIST OF TABLES……...xi

1 Introduction 1

1.1 Motivation 1

1.1.1 Literature Review 2

1.2 Propellor Aerodynamics and Acoustics 7

1.2.1 Introduction 8

1.2.2 Noise 10

1.2.3 Problem Statement and Objectives 13

2 Methodology 14

2.1 Governing Equations 14

2.1.1 Navier Stokes Equations 14

2.2 K-Ω SST and DES Model 16

2.3 Computational Approach 18

2.3.1 Grid Generation 18

2.3.2 Solver 25

2.3.3 Boundary Treatments 26

2.3.4 Flow Initialization 26

3 Results and Discussion 27

3.1 Isolated Rotor 28

3.2 Homogenous Ground Effects 35

3.3 Non-Homogeneous Ground Effects 39
4 Acoustics 46
4.1 Acoustic Data Collection 46
4.2 Isolated Rotor Acoustics 49
4.3 Homogeneous Ground Acoustics 53
4.4 Non-Homogeneous Ground Acoustics 56
4.5 Far Field Noise 58
5 Conclusion and Future Work 64
6 References 66

LIST OF FIGURES

Figure Page

1.1 Thrust Data VS blade type Deters [24] 3

1.2 Velocity Profiles of Propeller at different heights [20] 4

1.3 Isolated rotor blade testing configuration [35] 6

1.4 DJI Phantom III full drone testing configuration [35] 6

1.5 Thrust values different RPMS and solvers [34] 7

1.6 Blade Geometry representation [26] 9

1.7 Noise Generated from a blade [2] 11

2.1 Isolated rotor CAD 19

2.2 Rotor Twist Distribution 19

2.3 Rotor Chord Distribution 19

2.4 Isolated Rotor Mesh Top View 20

2.5 Tuna Can with Propeller Mesh 20

2.6 Isolated rotor Edge View 20

2.7 Isolated rotor Edge View 20

2.8 Isolated Rotor Z View 21

2.9 Isolated Rotor Y View 21

2.10 Homogeneous Ground Effects Z 21

2.11 Homogeneous Y View 21

2.12 Partial Ground Effects Z View 22

2.13 Partial Ground Effects Y View 22

2.14 Isolated Rotor Spanwise View 22

2.15 Representation of BlockMesh [21] 23

2.16 Check Mesh Full Ground Z view....24
2.17 Check Mesh rotor close up....25
3.1 Isolated Propeller 30 revolutions....28
3.2 Isolated Propeller Afari [2]....28
3.3 Vorticity Plot Z view....29
3.4 Vorticity plot Afari [2]....29
3.5 Vorticity plot [15]....30
3.6 Vorticity plot X view....30
3.7 Pressure Plot X view....31
3.8 Velocity plot X view....31
3.9 Pressure Results Z view Isolated propeller....32
3.10 Pressure distribution Polar Plot (leading edge)....32
3.11 Pressure distribution Polar Plot (Trailing edge)....33
3.12 Thrust V.S Time Isolated Porpeller....34
3.13 Moment V.S Time Isolated Propeller....34
3.14 Pressure x View Homogeneous Ground Effect....35
3.15 Pressure Z view Homogeneous Ground Effects....36
3.16 Velocity X View Homogeneous Ground Effect....36
3.17 Velocity Z View Homogeneous Ground Effect....37
3.18 Velocity Profiles at Different Heights Mora [25]....37
3.19 Thrust V.S Time Full Ground....38
3.20 Moment V.S Time Full Ground....39
3.21 Velocity Z Partial Ground Effects....40
3.22 Velocity X Partial Ground Effects....40

3.23 Partial Ground Effects at Different Heights Mora [25] 41

3.24 Vorticity Z Partial Ground Effects.....42

3.25 Vorticity X Partial Ground Effects 42

3.26 Pressure Z Partial Ground Effects.....43

3.27 Pressure X Partial Ground Effects 43

3.28 Total Force V.S Time Partial Ground.....44

3.29 Total Force V.S Time Partial Ground.....44

4.1 Probe locations for Near Field Acoustic Collection 47

4.2 Approx. Probe Locations Full Ground.....48

4.3 Approx. Probe Locations Partial Ground.....48

4.4 Probe Pressure Data V.S Time Isolated Rotor for First Probe Location 49

4.5 Probe Pressure Data V.S Time Isolated Rotor for Second Probe Location.....50

4.6 Probe Pressure Data V.S Time Isolated Rotor for Third Probe Location.....50

4.7 Sound Pressure Level Isolated Rotor [16] 51

4.8 Sound Pressure Level V.S Frequency Isolated Rotor.....52

4.9 Noise Levels for Real World Applications [33] 53

4.10 Probe Pressure Data V.S Time Full Ground Effects Rotor 53

4.11 Probe Pressure Data V.S Time Full Ground Effects Rotor for Second 54

4.12 Probe Pressure Data V.S Time Full Ground Effects.....54

4.13 Pressure probe Data 55

4.14 Sound Pressure Level V.S Frequency Ground Effects Rotor 55

4.15 Near Field Full Ground lower probe location.....56

4.16 Sound Pressure Level V.S Frequency Partial Ground Effects Rotor.....57

4.17 FWH Surface different Views 62

4.18 Endcaps Different Views 62

4.19 Pressure Distribution Across the Rotor Top and Bottom View Afari [2].....63

4.20 Pressure Distribution Across the Rotor Bottom View.....63

4.21 Pressure Distribution Across the Rotor Top View 64

LIST OF TABLES

Table Page

2.1 Boundary Conditions Ground Interactions 27

2.2 Boundary Conditions Isolated Propeller 27

3.1 Thrust Comparison Isolated Rotor with [24] 35

3.2 Thrust Ground Effects Compared to Isolated Rotor 39

3.3 Thrust Data for Partial Ground Effects 45

4.1 Probe locations Isolated Rotor 47

4.2 Probe Locations Full Ground 48

4.3 Probe locations Partial Ground 49

4.4 Upstream Probe Noise Level Comparison 58

1 Introduction

The following Chapter serves to introduce and highlight the new project below is a brief introduction of the motivation behind this work. This is expounded upon in later sections. Following this an in-depth look at the prior work accomplished during this project is looked into to provide valuable insight into the prior work accomplished.

1.1 Motivation

The integration of unmanned aerial vehicles (UAVs) into urban environments has become a reality, with numerous companies highlighting their capabilities in developing and deploying quiet and efficient Urban Air Mobility (UAM) systems. This new field holds considerable promise for advancing short-range aerial transportation infrastructure. However, the advent of this technology also brings forth a significant number of unknowns and uncertainties.

Among these uncertainties are the potential effects stemming from acoustic noise associated with Vertical Take-Off and Landing (VTOL) craft, as well as various aerodynamic challenges. These challenges manifest in the form of turbulent flow disturbances generated by the unsteady nature of urban environments, which can induce significant instabilities in the wake region of buildings and substantially influence conditions around these areas. Of particular concern is the intricate interplay between propeller operation and the surface during hover, a challenge not unique to UAM systems but prevalent in them. Understanding the ramifications of landing on and approaching rooftops is crucial for ensuring the safety of individuals in proximity to these aircraft.

Given the considerable interest in these areas and the safety concerns, it is imperative to conduct research aimed at comprehensively understanding the aerodynamic behaviors of electric Vertical Take-Off and Landing Systems (eVTOLs). Such endeavors are essential for enabling

accurate predictions and informed decision-making regarding the operation and safety protocols of these evolving technologies.

1.1.1 Literature Review

A considerable body of research has delved into the dynamics of isolated and ground effects pertinent to rotor systems. Notably, several investigations in this domain were conducted at Embry-Riddle Aeronautical University by Samuel Afari [2], establishing a foundational framework for the study of isolated Urban Air Mobility (UAM) systems. Afari's research focused on understanding the performance and acoustic characteristics of a solitary DJI Phantom rotor blade, employing a customized iteration of the Spalart-Allmaras turbulence model a departure from the kOmegaSST model adopted in the present study. Noteworthy is Afari's [2] use of switching between an Unsteady Reynolds-Averaged Navier-Stokes (URANS) to Large Eddy Simulation (LES), a transition discussed comprehensively in his work.

Further contributions to this domain include the empirical investigations conducted by Deters [24], which demonstrate experimental outcomes across different rotor configurations and their corresponding thrust performances. Deters' experimentation encompassed an array of ten distinct rotor configurations, powered by four different motors, facilitating a comprehensive analysis of isolated rotor dynamics. Deters' study reported an anticipated thrust magnitude of approximately 4 newtons for the DJI blade, with other assessments for other alternative blade designs. These experimental endeavors were conducted at Embry-Riddle Aeronautical University, with attention to measurement precision, ensuring propeller sizing accuracy to the nearest 0.05 inches. However, the rotor profiles do differ slightly due to the implementation of various scanning software’s that do not provide absolute accuracy.

The propulsion apparatus employed in these experiments comprised of off-the-shelf motors sourced from various manufacturers. The data acquisition was facilitated using a calibrated thrust

curve, converting voltage outputs from a Data Acquisition (DAQ) system into corresponding force values. This calibration was achieved through empirical validation via a pulley system, establishing a relationship between force and voltage outputs, ensuring the integrity and reliability of the acquired thrust data.

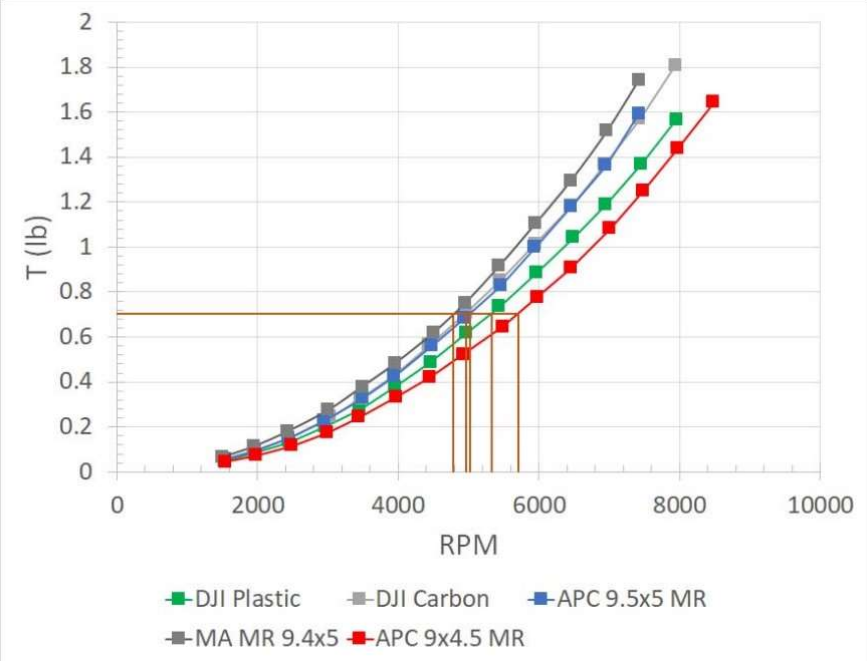

Figure 1.1 Thrust Data VS blade type Deters [24]

The field of ground effects research pertaining specifically to the DJI Phantom II remains relatively underexplored, with limited studies addressing the intricacies of this phenomenon. However, broader investigations into the effects of ground proximity encompassing both partial and homogeneous ground effects have been conducted. It is anticipated that research in this domain will follow the same trend as the current propeller, albeit with divergent numerical results.

Significant contributions to this have been made by Mora [20], whose research delved into the dynamics of helicopters approaching aircraft carriers and the consequential impact of ground effects as rotor blades interface with the carrier deck. Mora's investigation entailed a comprehensive

examination of the velocity profile exhibited by these rotor blades during approach maneuvers. Notably, Mora's work demonstrated variations in blade velocity profiles on the deck of the aircraft carrier, as depicted in Figure 1.2 for illustrative comparisons.

While the specifics of Mora's research focus on rotorcraft operations in the context of aircraft carrier landings, the underlying principles hold relevance to the broader discourse surrounding ground effect dynamics in rotorcraft operations. By demonstrating the interaction between rotor blade dynamics and ground proximity, Mora's research contributes valuable insights into the complex aerodynamic phenomena governing rotorcraft operations in close proximity to surfaces.

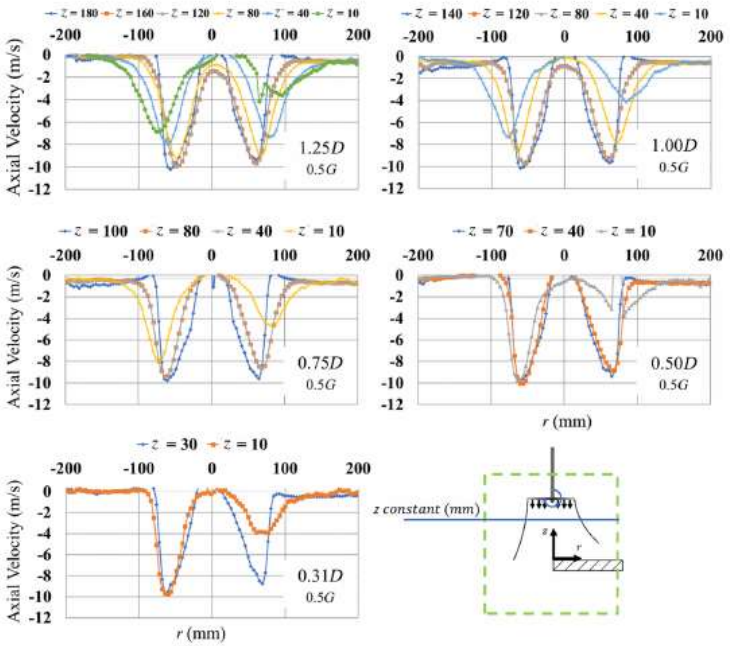

Figure 1.2 Velocity Profiles of Propeller at different heights [20]

Numerous studies have been undertaken in the realm of rotor blade aerodynamics, yet scant attention has been dedicated to the specifics of the DJI Phantom III rotor blade. This impedes the establishment of valid comparisons, necessitating a comprehensive investigation to validate isolated results obtained thus far. To address this gap, the present study attempts to compare the results of

isolated results with that of current experimentation, then employ a meshing approach closely aligned with the isolated rotor. Such methodological consistency is anticipated to enhance understanding of CFD software and facilitate meaningful comparisons across studies.

A pivotal aspect of this research pertains to the gathering of aeroacoustics characteristics derived from computational simulations. Extensive research has been conducted in the field of aeroacoustics, particularly concerning isolated propeller configurations. Notable among these studies is the seminal work by Afari [2], wherein a modified iteration of the Spalart-Allmaras turbulence model was employed to model flow fields, with probe locations and Ffwocs-Williams Hawkings (FWH) surfaces utilized for comprehensive pressure data acquisition throughout simulations. Afari's simulations encompassed predictions of both far-field and near-field acoustics, facilitated by grid spacing conducive to capturing frequencies up to 1700 Hz. While Afari's investigations focused on isolated rotor dynamics, they serve as a valuable resource for acoustic comparisons in the present study.

By using insights gleaned from Afari's work and adopting similar modeling methodologies, the present research aims to shed light on the aeroacoustics implications of DJI Phantom III rotor blade configurations. This comparative approach holds promise for understanding and demonstrating the acoustic signatures associated with these rotor systems, thereby enriching the understanding of their aerodynamic and acoustic characteristics.

Further research was conducted at Nasa Ames by [35]. This research sought to understand and compare the different performance characteristics of varying types of drones. Of these drone types compared the DJI Phantom III rotor was researched. This rotor is the most up to date version of the rotor and due to this does vary slightly from the rotor configuration used. However, the values recorded in this study should fall in the general range of this test completed. The test stand

configuration can be seen in Figure 1.3 and Figure 1.4 below. The tested predicts values of thrust of 4.8 Newtons per rotor blade for the rotor type tested.

Figure 1.3 Isolated rotor blade testing configuration [35]

Figure 1.4 DJI Phantom III full drone testing configuration [35]

Finally computational tests where completed by Thai and Grace [34] comparing computational results with the results at the experiment by [35]. The experiment used 2 different software's and

the various solvers associated with the software. The main solver of interest here is the $k\omega$ solver this solver underpredicted the values from the experiment. The thrust values can be seen in Figure 1.5 highlighted in blue. The RPM values tested here as well as the rotor twist distribution shown are different from the current simulation. The RPM tested here are 3, 5 and 7 thousand as can be seen in Figure 1.5. This simulation also provided the basis for calculating Figure of Merit (F.O.M) this is covered in more detail in the following section.

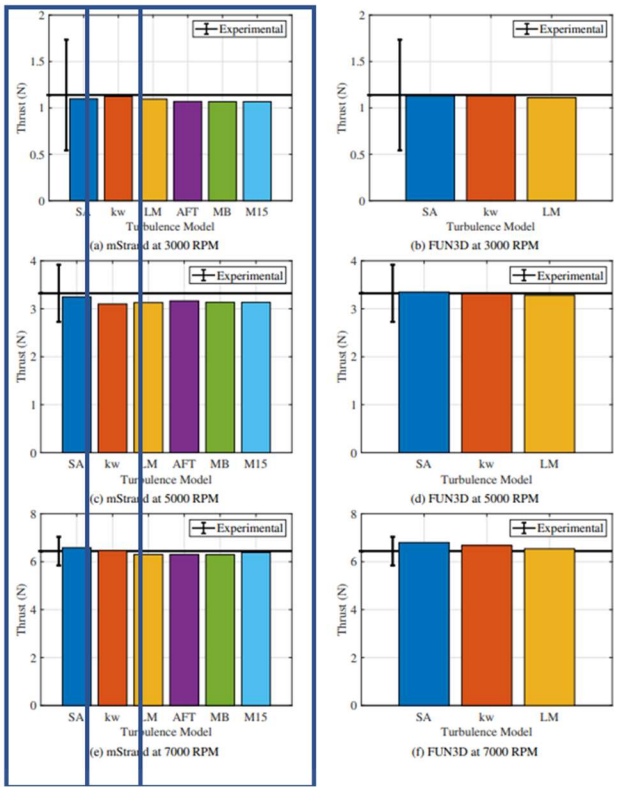

Figure 1.5 Thrust values different RPMS and solvers [34]

1.2 Propellor Aerodynamics and Acoustics

The following section serves to discuss the implementation and the important problems that the current work is attempting to solve. This section serves as a brief introduction to the current work and also general background to both noise and acoustics.

1.2.1 Introduction

Unmanned Aerial Vehicle (UAV) aerodynamics closely parallel those of helicopters, falling within the domain of rotorcraft aerodynamics. The prediction of forces acting on a given propeller typically involves employing mathematical computations to anticipate blade surface interactions, accounting for various simulation factors. While the primary focus of this research lies elsewhere, it remains essential to elucidate the foundational principles underpinning propeller design and the associated design parameters.

Fundamental to propeller design are factors such as blade twist (τ), blade thickness (T), and chord root (Cr), alongside operational parameters including rotations per minute (rpm) and upstream velocity. Notably, numerous studies have explored the optimization of propeller configurations based on chord and twist distributions. For instance, a study by Joanne L. Walsh [26] delves into the development of methodologies for optimizing rotor design in helicopter blades. This research shows the impact of adjusting chord length, twist distribution, and tip geometry on blade performance, as well as the effects of manipulating rpm and blade count. Figure 1.6 provides a graphical representation of these parameters, employing distinct symbols to delineate their respective characteristics.

By considering these fundamental design parameters and leveraging insights from prior optimization studies, the present research aims to contribute to a deeper understanding of UAV aerodynamics and propeller behavior. Such endeavors hold promise for advancing the efficiency and performance of UAV systems through informed design strategies and parameter optimization.

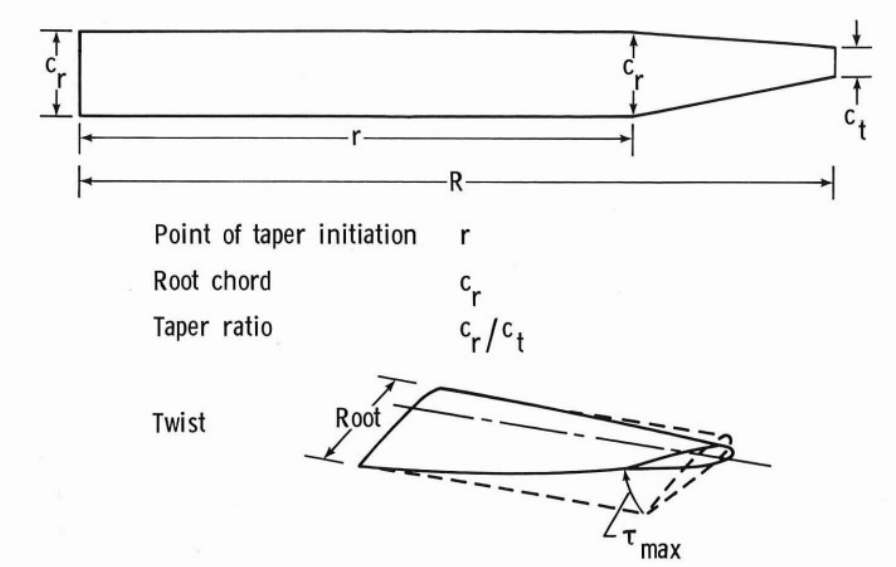

Figure 1.6 Blade Geometry representation [26]

Figure 1.6 provided above shows key design parameters essential for propeller configuration, namely, the point of taper initiation (denoted as "r"), root chord, taper ratio (TR), and maximum twist. The point of taper initiation signifies the point where the tapering of the blade initiates. Until this the blade maintains a rectangular profile, following which it linearly tapers towards the tip. The taper ratio (TR) quantifies the ratio of the chord at the point of taper initiation (cr) to the chord at the tip (c_t), providing insight into the degree of tapering along the blade span. Furthermore, the blade's twist distribution varies linearly from the root to the tip, culminating in its maximum twist value (τ_{max}) at the blade's end. The current propellers parameters and twist distribution will be expounded upon in subsequent sections, as outlined in the methodology [26].

Once a blade configuration is established, the computational assessment of thrust performance becomes important. Thrust calculation is inherently numerical, leveraging the chosen simulation model to derive accurate predictions. The thrust force is determined by the pressure distribution across the airfoil, as defined by equations (22,23), facilitating the quantification of thrust generation and performance characteristics.

$$F_p = \sum \rho_i s_{f,i}(p_i - p_{ref}) \quad 1.1$$

$$F_v = \sum s_{f,i} \cdot (\mu R_{dev}) \quad 1.2$$

Here ρ_i is the density, $s_{f,i}$ is the face area vector, μ is the dynamic viscosity, and R_{dev} is the stress tensor. After thrust is calculated from the results the coefficient of thrust needs to be measured to allow better comparison. To calculate C_t equation 1.3 is used. This allows valid comparison of rotor types as well as allowing the current research to be compared to prior work to ensure accurate data analysis.

$$C_t = \frac{T}{\rho * \pi * r^2 * (\omega * r)^2} \quad 1.3$$

Where T is the thrust r is the radius of the blade and ω is the rotation rate [34]. Following this it's important to calculate the Figure of Merit (F.O.M) for all rotor configurations first torque coefficient needs to be evaluated:

$$C_q = \frac{M}{\rho A \Omega^2 R^3} \quad 1.4$$

Figure of Merit is then evaluated:

$$\eta = \frac{C_t^{\frac{3}{2}}}{\sqrt{2C_q}} \quad 1.5$$

1.2.2 Noise

The noise generation mechanisms depend heavily on the aircraft's configuration, with aspects such as rotor blade shape variations affecting airflow, vortex formation, and ultimately noise through pressure changes. Rotor noise is typically divided into tonal, influenced by blade geometry and aerodynamic forces, and broadband (BBN) arising from diverse sources such as airfoil-induced turbulence, rotor-blade interactions, and atmospheric turbulence. Tonal noise further divides into thickness noise, produced by the rotating blade, and loading noise, resulting from lift and drag. In advancing flight, the radiation pattern of noise shifts due to azimuthal fluctuations and factors such as tip-path-plane angles [3]. Blade-vortex interaction (BVI) noise emerges from rapid pressure changes on rotor blades due to the tip vortices of the preceding blades, especially noticeable during descent. BBN, characterized by localized pressure fluctuations, gains prominence in e-VTOLs due to reduced design tip Mach numbers.

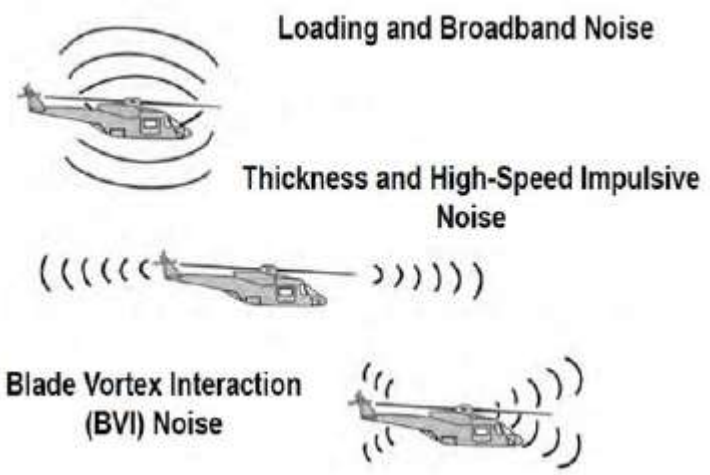

Figure 1.7 Noise Generated from a blade [2]

Predictive methodologies for propeller and rotor analysis have evolved significantly. Initially, simple models like the actuator disk theory and the Rankine-Froude model [4] conceptualized the rotor as a thin disk in uniform inflow, idealizing fluid behavior for basic thrust and power

estimation. Early acoustic theories, capable of predicting tonal noise at initial harmonics, also emerged during this period [5, 6]. Advancements led to the Blade Element theory, BET [7], which considered variations in thrust and torque along the rotor radius. This theory, combined with earlier models, evolved into the BEMT, enhancing the prediction of inflow velocities, and loading distribution. BEMT's accuracy in steady thrust loading prediction, especially when integrated with CFD methodologies, has been well-documented [8, 9]. Further refinements, such as Prandtl-Glauert tip-corrections [10], improved aerodynamic predictions. XFOIL [11], a lower fidelity but quick-response aerodynamic modeling tool, complements BEMT in various applications. High-fidelity approaches, for instance, the hybrid Large Eddy Simulation (LES)-Unsteady Reynolds Averaged Navier Stokes (RANS) model, have been employed for more complex scenarios, such as single and multirotor aerodynamics in hover [2, 12, 13]. The approach was further extended to study counter-rotating propellers, revealing insights into aerodynamics [14–17]. Another hybrid RANS/LES study on a quadcopter propeller's wake dynamics found consistency between turbulence models, except for the turbulence viscosity field in distant wakes [18].

Lighthill's work was expanded to consider moving solid boundaries, resulting in the Ffowcs Williams-Hawkings Equation (FW-H) covering areas such as rotor noise and impinging jet noise [19]. The FW-H method requires pressure, velocity, density, and time derivatives to be collected on a surface that encloses most of the noise sources. At first, an impermeable surface was considered. However, this method was applied to permeable surfaces later, which improved its versatility, and it is now the prevailing method to extend near-field CFD results to the acoustic far-field. The placement of the collection surface and the grid refinement plays a vital role in the acoustic results of such methods, hence a convergence study over these parameters must be done. The PSU-WOPWOP software suite is preferred for noise prediction [20]. It utilizes the Ffowcs Williams-Hawkings (FW-H) equation to model and propagate noise sources, providing accurate SPL

estimations. The primary focus of this study is to analyze the impact of far-field noise on an e-VTOL operating in a nonhomogeneous vertiport environment. This work serves as inspiration for a better understanding of the e-VTOL dynamics around buildings, as it can enable the development and implementation of this type of vehicle in populated areas.

1.2.3 Problem Statement and Objectives

The following research serves to compare the changes in thrust and acoustics on an isolated rotating propeller when a Homogeneous and Non-Homogeneous ground is implemented below the propellor. This research aims at better understanding UAVS and the urban environments in which they operate. The current objectives of this research are as follows.

1. Study aerodynamic forces and acoustics off an isolated propellor. (Rotor only)
2. Study aerodynamic forces and acoustics off a propellor hovering above a homogenous surface. (Full ground effects)
3. Study aerodynamic forces and acoustics due to the implementation of a non-homogenous surface. (Partial ground effects)
4. Finally, to compare these results to better understand VTOLs in an urban environment.

2 Methodology

There are many approaches available to evaluate noise and performance parameters of a rotor. Work done by Afari [2] provided a very complex and detailed explanation of how a model like the spallartallmars model can be used and adapted to determine the acoustic forces present in a complex hybrid simulation. This hybrid simulation type is still used by current research but a sperate model is used known as the KomegaSST model this model demonstrated by Menter [30] will be discussed in further detail but allows no further code modification. In the following section the governing equations used, along with the models used for simulation are discussed. With this the grid generation along with the boundary treatment used will be demonstrated. A hybrid approach to computational fluid dynamics is used. This approach allows for both computational costs to be minimized but accuracy to be allowed [27].

2.1 Governing Equations

Within the computational domain, both the unsteady flow field and the near-field acoustic field are resolved numerically. Employing a Hybrid LES-URANS (HLU) approach, akin to the methodology previously utilized by [27], URANS is implemented in proximity to solid surfaces. This choice is made due to the prohibitive computational demands associated with achieving LES resolution necessary to resolve the boundary layer in these regions. Conversely, LES is employed in other areas of the domain. This also follows a very similar procedure demonstrated by Afari [2].

2.1.1 Navier Stokes Equations

The Navier stokes equations are the base model equations for the entire domain used in this computational set up. The equations were derived independently by Stokes and Navier [28], in the early 1800's The basic equations take the following form.

$$\frac{\partial \rho}{\partial t} + \frac{\partial (\rho u)}{\partial x} + \frac{\partial (\rho v)}{\partial y} + \frac{\partial (\rho w)}{\partial z} = 0 \tag{2.1}$$

$$\frac{\partial (\rho u)}{\partial t} + \frac{\partial (\rho u^2)}{\partial x} + \frac{\partial (\rho uv)}{\partial y} + \frac{\partial (\rho uw)}{\partial z} = -\frac{\partial p}{\partial x} + \frac{1}{Re_r}\left[\frac{\partial \tau_{xx}}{\partial x} + \frac{\partial \tau_{xy}}{\partial y} + \frac{\partial \tau_{xz}}{\partial z}\right] \tag{2.2}$$

$$\frac{\partial (\rho v)}{\partial t} + \frac{\partial (\rho uv)}{\partial x} + \frac{\partial (\rho v^2)}{\partial y} + \frac{\partial (\rho vw)}{\partial z} = -\frac{\partial p}{\partial y} + \frac{1}{Re_r}\left[\frac{\partial \tau_{xy}}{\partial x} + \frac{\partial \tau_{yy}}{\partial y} + \frac{\partial \tau_{yz}}{\partial z}\right] \tag{2.3}$$

$$\frac{\partial (\rho w)}{\partial t} + \frac{\partial (\rho uw)}{\partial x} + \frac{\partial (\rho wv)}{\partial y} + \frac{\partial (\rho w^2)}{\partial z} = -\frac{\partial p}{\partial z} + \frac{1}{Re_r}\left[\frac{\partial \tau_{zx}}{\partial x} + \frac{\partial \tau_{zy}}{\partial y} + \frac{\partial \tau_{zz}}{\partial z}\right] \tag{2.4}$$

These are the familiar base model equations first derived that initiate the procedure for solving the flow in the space. The equations are the continuity equation the X, Y, Z momentum equations respectively. These equations need to be further derived and changed to allow for the addition of compressible flow [27].

$$\frac{\partial \rho}{\partial t} + \frac{\partial \left(\rho u_j\right)}{\partial x_j} = 0 \tag{2.5}$$

$$\frac{\partial (\rho u_i)}{\partial t} + \frac{\partial}{\partial x_j}\left[\rho u_i u_j + p\delta_{ij} - \tau_{ij}\right] = 0 \tag{2.6}$$

$$\frac{\partial (\rho e_t)}{\partial t} + \frac{\partial}{\partial x_j}\left[\rho u_i e_t + p u_j + q_j - u_j \tau_{ij}\right] = 0 \tag{2.7}$$

$$\tau_{ij} = 2\mu S_{ij} - \frac{1}{3}\frac{\partial u_k}{\partial x_k}\delta_{ij} \tag{2.8}$$

$$e_t = e + \frac{u_k u_k}{2} \tag{2.9}$$

In the above equations q_j is the heat flux e_t is the total energy τ_{ij} is the viscous stress, k is the thermal conductivity, and μ is Sutherlands law of viscosity and S_{ij} is the strain tensor both given below:

$$S_{ij} = \frac{1}{2}\left(\frac{\partial u_i}{\partial x_j} + \frac{\partial u_j}{\partial x_i}\right) \tag{2.10}$$

$$q_j = -k\frac{\partial T}{\partial xj} \equiv -C_p\frac{\mu}{Pr}\frac{\partial T}{\partial x_j} \tag{2.11}$$

$$\mu(T) = \frac{\mu_0(T_0 + C)}{T + C}\left(\frac{T}{T_0}\right)^{\frac{3}{2}} \tag{2.12}$$

Where Pr is the Prandtl Meyer number μ_0, T_0, C, are all reference values with each being the dynamic viscosity temperature and Sutherlands constant for air.

2.2 K-Ω SST and DES Model

The simulation is initiated in a base model k- ω Shear Stress Transport equation this is a two-equation model that aims at solving the turbulence kinetic energy, k, and turbulence specific dissipation rate, ω. This model overcomes the deficiencies in the initial k- ω model with respect to the reliance of the freestream values. This model can capture flow separation and was initially utilized in a variant of OpenFoam from 2003 this model is based off of work from Gou [7] and was shown to have reliable results. The turbulence specific dissipation is given by:

$$\frac{D}{Dt}(\rho\omega) = \nabla\cdot(\rho D_\omega\nabla\omega) + \frac{\rho\gamma G}{\nu} - \frac{2}{3}\rho\gamma\omega(\nabla\cdot\mathbf{u}) - \rho\beta\omega^2 - \rho(F_1 - 1)CD_{k\omega} + S_\omega \tag{2.13}$$

The turbulent kinetic energy:

$$\frac{D}{Dt}(\rho k) = \nabla \cdot (\rho D_k \nabla k) + \rho G - \frac{2}{3}\rho k(\nabla \cdot \boldsymbol{u}) - \rho \beta^* \omega k + S_k \quad 2.14$$

The turbulent viscosity:

$$\nu_t = a_1 \frac{k}{\max(a_1 \omega b_1 F_{23} \boldsymbol{S})} \quad 2.15$$

These values are then initialized first for the kinetic energy assuming I is intensity and $\mathbf{u}_{ref}$ is reference velocity. Also, where C_μ is a constant at 0.09 and L is the reference length scale:

$$k = \frac{3}{2}\left(I|\boldsymbol{u}_{ref}|\right)^2 \quad 2.16$$

$$\omega = \frac{k^{0.5}}{C_\mu^{0.25} L} \quad 2.17$$

After this model is ran for 20 revolutions the model is then switched to an LES model specifically a Detached Eddy Simulation (DES) model The usability and the adaptation of the DES model is discussed in great detail by [30] where it is shown the benefits of using a hybrid model like this. This model adjusts the length scale present in the simulation by replacing it with a switching function. The model does not change in its approach to solving the turbulent specific dissipation rate but does alter course in the turbulent kinetic energy:

$$\frac{D}{Dt}(\rho k) = \nabla \cdot (\rho D_k \nabla k) + \min(\rho G, (c_1 \beta^*) \rho k \omega) - \frac{2}{3}\rho k(\nabla \cdot \boldsymbol{u}) - \rho \frac{k^{1.5}}{\bar{d}} + S_k \quad 2.18$$

The length scale $\bar{d}$ is given:

$$\min\left(C_{DES}\Delta, \frac{\sqrt{k}}{\beta^{*}\omega}\right) \tag{2.19}$$

The turbulent viscosity stays the same. Initializing with URANS saves computational time and the switch to the DES model is quite simple using OpenFOAMs interface.

2.3 Computational Approach

The following section explains the approach used in this simulation. The gridding method along with the program used for meshing. Including the boundary conditions given and the flow initialization for all geometry types. This section provides a robust overview of the process of creating a usable mesh in OpenFOAM.

2.3.1 Grid Generation

The primary challenge addressed in this research pertains to the generation of a grid capable of yielding valid results. The 9450 propeller, is a widely utilized commercial propeller subjected to numerous experiments, serves as the focal point of this study, comprising three distinct hovering rotor aerodynamic simulations.

Initially, an isolated rotor scenario is simulated, with the rotor positioned amidst non-reflecting boundaries and surrounded by a wake refinement zone above and below the rotor. This configuration serves as a benchmark for subsequent simulations. Subsequently, a building is introduced into the simulation as a wall positioned beneath the rotor, constituting a homogeneous ground effect case. Finally, the rotor is positioned at the building's edge, simulating a non-homogeneous case characterized by a half-plane beneath the rotor.

The rotor under investigation is the two-bladed type 9450 model as depicted in Figure 2.1, commonly featured on the commercially available DJI Phantom III drone. With a diameter (D)

measuring 0.239 meters and a tip chord (C_{tip}) of 0.01 meters, this rotor's chord, and twist distributions, as documented in literature [15], were utilized to generate a Computer-Aided Design (CAD) model, as showcased in Figure 2.1. Notably, this CAD model has been previously employed in a 3D Computational Fluid Dynamics (CFD) analysis [14].

(a) (b)

Figure 2.1 Isolated rotor CAD

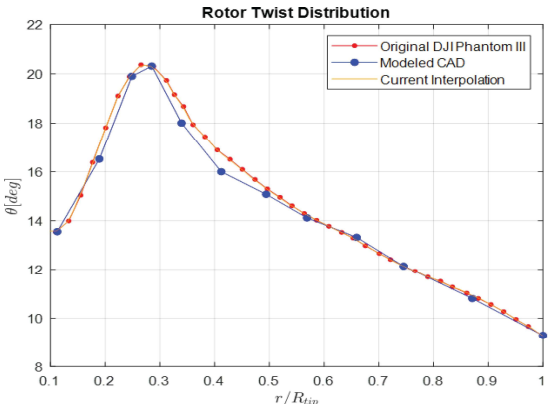

Figure 2.2 Rotor Twist Distribution

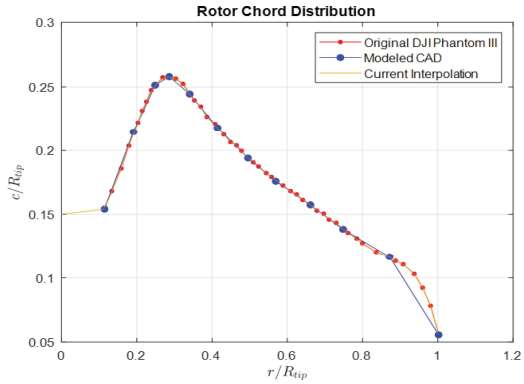

Figure 2.3 Rotor Chord Distribution

In the homogeneous case, the building is positioned at a distance of 1.25 times the rotor diameter (1.25D) away from the rotor. Conversely, the non-homogeneous case involves aligning the rotor center with the edge of the building.

For the initial isolated rotor scenario, a cylindrical AMI rotating mesh grid is employed. Commonly referred to as a "Tuna can" due to its cylindrical shape resembling a can of tuna, this configuration allows the rotor to rotate freely within the cylinder. However, as the cylinder terminates and transitions into the wake zone, the mesh ceases rotation, ensuring the appropriate propagation of information throughout the remainder of the mesh.

Figure 2.4 Isolated Rotor Mesh Top View

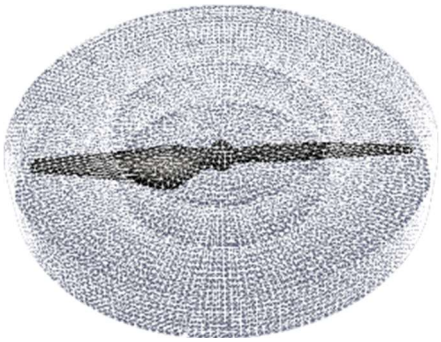

(a)

Figure 2.5 Tuna Can with Propeller

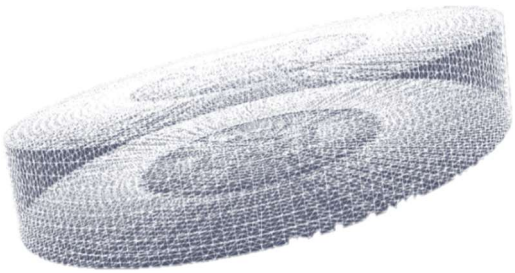

(b)

Figure 2.6 Isolated rotor Edge View

Figure 2.7 Isolated rotor Edge View

After and above the "tuna can," a wake region forms for the isolated rotor. This wake region extends to the end of the domain, which is 0.81 meters away from the center of the rotor and extends out from the rotor by 2.5 radii.

In the ground case, the rotor is positioned 1.25 diameters above the ground, and the wake region maintains the same distance from the rotor but stops at the roof top.

Finally, for the half ground or non-homogeneous case, the rotor is positioned 1.25D away from the ground and exactly splits the ground and the open surface. The wake maintains the same distance of 2.5 radii away, but it conforms to the geometry of the half building see Figure 2.12.

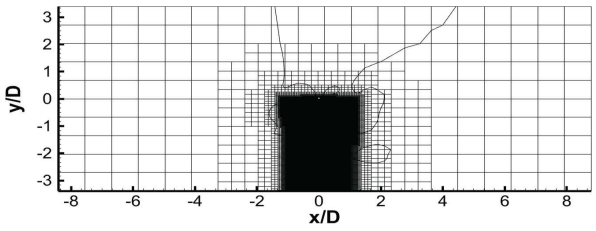

Figure 2.8 Isolated Rotor Z View

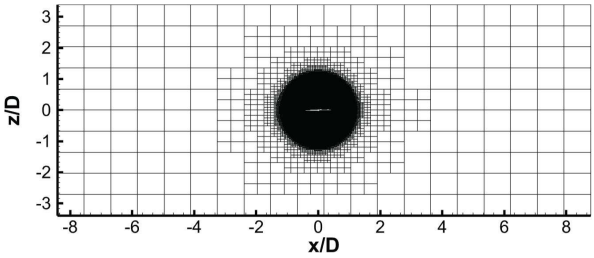

Figure 2.9 Isolated Rotor Y View

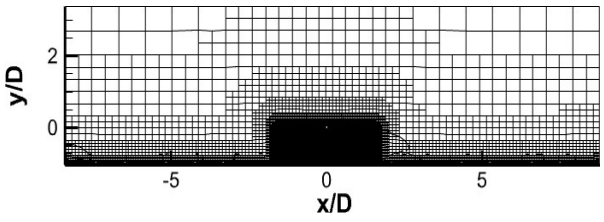

Figure 2.10 Homogeneous Ground Effects Z

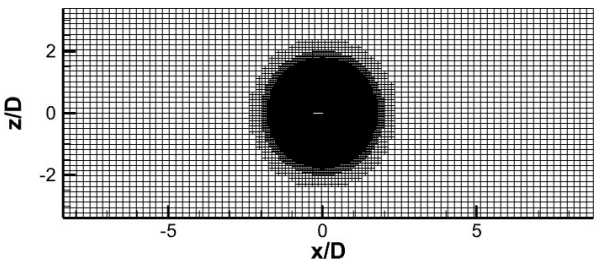

Figure 2.11 Homogeneous Y View

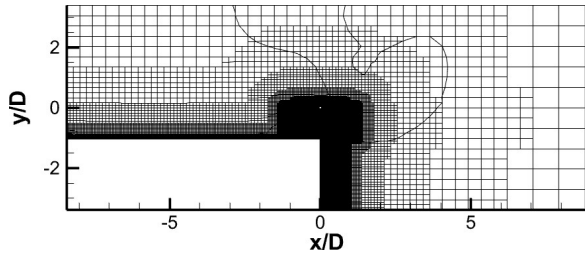

Figure 2.12 Partial Ground Effects Z View

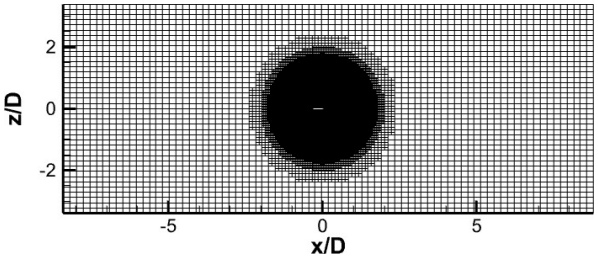

Figure 2.13 Partial Ground Effects Y View

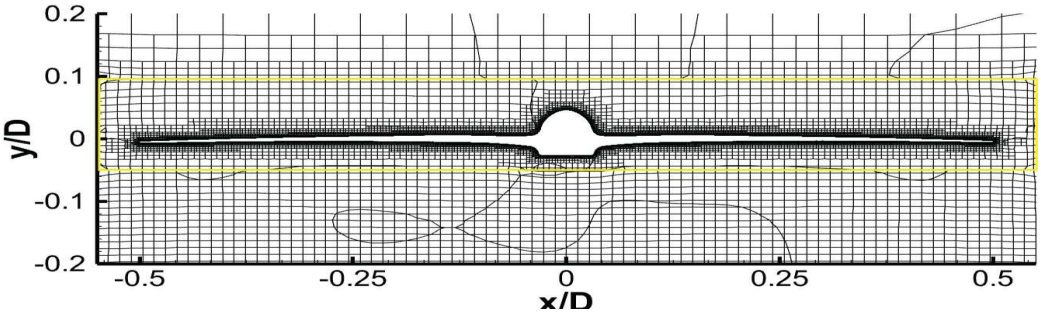

Figure 2.14 Isolated Rotor Spanwise View

This mesh was generated using OpenFOAM's local meshing utility, called snappyHexMesh, in conjunction with blockMesh. The blockMesh tool defines the bounding box, while snappyHexMesh operates by utilizing an uploaded geometry file to extract the object from the internal mesh. The internal mesh, referred to as a block mesh, is configured with parameters and boundary conditions, which will be elaborated upon later.

These features are defined with a specific refinement level, which differs from other meshing software that allows for the explicit setting of y+ values. Consequently, meshing becomes somewhat of an art form. For this particular geometry, the refinement level is set to 10 on the propeller. This entails dividing each part of the mesh that touches the propeller 10 times, resulting in a local average y+ of 1.8.

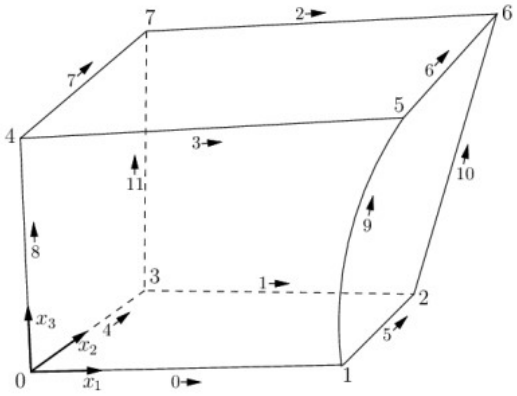

Figure 2.15 Representation of BlockMesh *[21]*

The wake region is refined to a level of 7, ensuring a y+ value of approximately 10 on the building's surface, thereby enabling proper resolution of the flow field along the wall. From this refined region, the mesh transitions to a level 1 refinement throughout the rest of the field, progressing in six steps downwards from level 7. This approach prevents improper growth and computational errors along the rotor. Additionally, the grid mesh extends 5 cm above the top of the rotor, encompassing the entire rotor assembly.

The overall grid cell sizes for each simulation are as follows: 30 million cells for the isolated rotor, 80 million cells for the partial building case, and 72 million cells for the full building scenario. Two additional test cases were conducted for both the regular building and the isolated propeller, each with cell counts of 8 million and 11 million respectively. Although these test cases maintained low y+ values on the rotor, they exhibited significantly reduced wake refinement regions, resulting in data loss.

Furthermore, attempts were made to achieve finer mesh resolution near the building walls, aiming for a y+ value closer to one. However, this endeavor led to impractical cell counts of around 200 million for both wall test cases. As a result, such fine mesh grids were deemed unfeasible.

After this a new mesh was generated to ensure accurate upstream data propagation. These meshes altered the current meshes by increasing the size of the wake region but reducing the y+ around both the building and the propeller. These meshes were generated mainly for acoustic data collection to better incorporate future Ffowcs-Williams Hawkings surfaces. This also allows for further comparison between the thrust, moment and near field acoustics. Providing another source of comparison between these values. These meshes also use the same computational approach and boundary treatments with the only difference being the chosen scheme for solving the flow. This mesh is referred to as check to differentiate in comparisons. Below in FIGURE is the full building generation of the mesh this follows the same process for all mesh configurations so only one mesh is shown. The mesh uses a process of layer generation which allows more accurate growth from a surface but at the cost of accuracy around the blade edge. Also a larger region around the blade is used with a lesser refinement level in order to capture better acoustics. The close up of the rotor blade is also shown in Figure 2.16

Figure 2.16 Check Mesh Full Ground Z view.

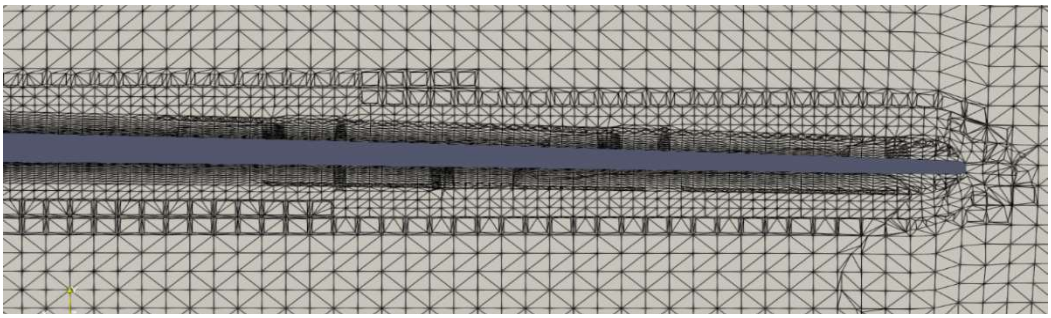

Figure 2.17 Check Mesh rotor close Up.

2.3.2 Solver

The solver used employs a code from OpenFOAM v1912 this code is called rhoPimpleFoam and it is pressure based and uses a pimple solver which is both transient and compressible. The pimple algorithm is a combination of both the Semi-Implicit Method for Pressure-linked Equations or SIMPLE and the Pressure Implicit with Splitting of Operator or PISO both solvers are explained in detail by Zikanov [29] in his book. These schemes are combined to create a solver that has 5 corrector loops per time step and 3 pressure corrector corrections per loop. This increases solver stability. OpenFOAM utilizes the finite volume method and allows integration between cell centers allowing for the Gauss theorem to convert the volume integrals into surface integrals. This is demonstrated and discussed in detail by Afari [2].

Finally, time advancement is done via the second order Crank-Nicholson scheme:

$$\frac{u_i^{n+1} - u_i^n}{\Delta t} = a^2 \frac{1}{2} * \frac{(u_{i+1}^n - 2u_i^n + u_{i-1}^n) + (u_{i+1}^{n+1} - 2u_i^{n+1} + u_{i-1}^{n+1})}{\Delta x^2} \qquad 2.20$$

The time step employed in this is based off a maximum courant number of 10 when this courant number is reached a time step of 3 x 10^{-6} is utilized. Then upon acoustic data collection a steady time step of the same value is used, and courant number is held at ten. The rotor is operated at a

constant rpm of 6000. This begins the URANS model then after 20 revolutions the run is switched to the LES model this model is ran for at least 10 iterations before acoustic data is collected. The time step is held constant throughout. This can be achieved due to the high computational power available at the NASA HECC cluster.

2.3.3 Boundary Treatments

In the isolated rotor simulation, only two main boundaries are considered: the propeller itself and the outer boundaries. The formulation is relatively straightforward, with the propeller treated as a no-slip wall, exhibiting zero pressure and temperature gradients. The outer edges of the computational domain are treated as wave transmissive, allowing the flow to pass through without interaction. This is verified by running the simulation until the flow reaches the lower outer boundary and passes through it.

Introducing buildings presents additional challenges in determining the boundary conditions for the simulation. Both buildings follow the same treatment as the wall, characterized by a no-slip condition and employing the same eddy viscosity treatment. However, due to the higher y+ value of 10, some data loss occurs along the wall. For the partial building scenario, both a transmissive boundary and a solid boundary are employed. The edge of the building runs the length of the lower boundary of the simulation, resulting in flow along this boundary. The entire half building is treated as a no-slip surface, while the lower wall is treated as transmissive. OpenFOAM's built-in wave transmissive function is utilized for this purpose, with a specified value provided.

2.3.4 Flow Initialization

The flow is initialized in URANS with an initial velocity, pressure, temperature, and density each aspect is given then the simulation is allowed to run. Below is a table outlining the initial conditions. For all mesh types of the mesh used for the isolated rotor is very similar to that of its

non-isolated counter parts with the glaring difference being in the implementation of the wall conditions.

Table 2.1 Boundary Conditions Ground Interactions

Boundary Conditions Ground Interactions					
Boundary	nut	T	P	U	nuTilda
Propellor	nutUSpaldingWall Function	zeroGradient	zeroGradient	Moving Wall Velocity (0 0 0)	fixedValue 0
Ground	nutUSpaldingWall Function	zeroGradient	zeroGradient	noSlip	fixedValue 0
Internal Fields	uniform 3.287*10−6	uniform 298.5	uniform 101325	uniform (0 0 0)	uniform 4.686*10−5

Table 2.2 Boundary Conditions Isolated Propeller

Boundary Conditions Isolated propeller					
Boundary	nut	T	P	U	nuTilda
Propellor	nutUSpaldingWall Function	zeroGradient	zeroGradient	Moving Wall Velocity (0 0 0)	fixedValue 0
outlet	Calculated 3.287*10−6	Wave Transmissive 298.5	Wave Transmissive 101325	Wave Transmissive (0 0 0)	fixedValue 4.686*10-5
Internal Fields	uniform 3.287*10−6	uniform 298.5	uniform 101325	uniform (0 0 0)	uniform 4.686*10−5

3 Results and Discussion

The following chapter discusses the results from the simulations ran. These simulations where ran on the NASA HECC cluster on the Broadwell Electra nodes with 1500 processors. These simulations where ran using parallel processing. The meshes where generated on the Vega cluster at Embry-riddle aeronautical university these were ran with 360 processors also in parallel then the

meshes were uploaded to the NASA cluster. This was to prevent a meshing error and wasting valuable computational time on the NASA cluster.

3.1 Isolated Rotor

Initial results from the isolated rotor simulation need to be compared with experimental data to validate the meshing. While there is limited experimental data available for ground effects with DJI rotors, isolated results are more readily accessible. Below, the results from an isolated rotor study conducted by Afari [2] are presented alongside the current findings for comparison.

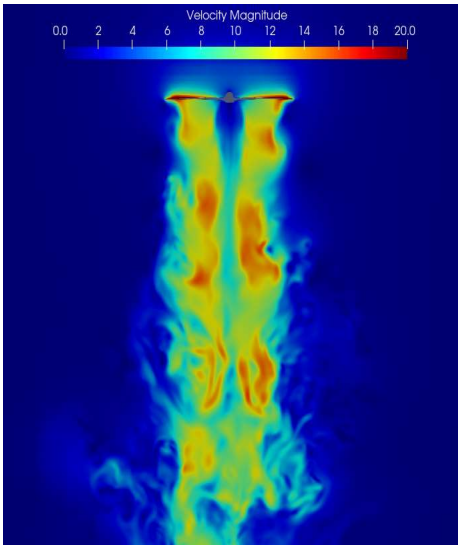

Figure 3.1 Isolated Propeller 30 revolutions

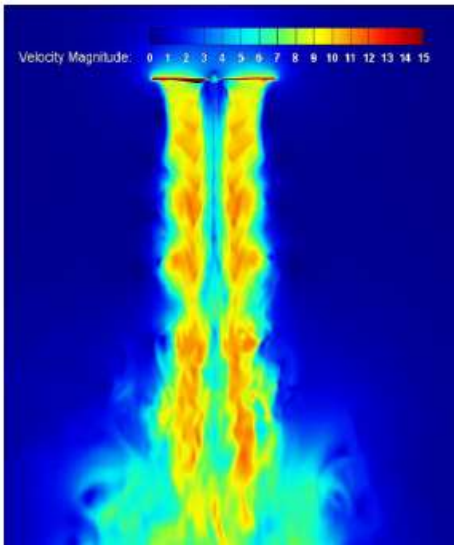

Figure 3.2 Isolated Propeller Afari [2*]*

The velocity plot contours for the isolated rotor exhibit a visually comparable trend between the results obtained in the current experiment and those documented by Afari [2]. It's noteworthy that a notable disparity exists in the duration of the simulations, with Afari's rotor running for over 40 revolutions compared to the 30 revolutions in the current experiment.

Similarly, the vorticity magnitude plots demonstrate a similar trend, with the maximum vorticity magnitude set at 2000. These findings are satisfactory on a visual level, validating the

initial simulation assumptions. Additionally, it's essential to acknowledge that Afari's results were obtained using a different DJI rotor type, implying that there may be slight differences in both magnitude and noise propagation between the two sets of results. Research conducted by Yoon and Diaz [15] was initially compared to results by [2] but in this research as can be seen below outlined in red there was a large disparity in the visual vorticity roll up between [2] and [15] this difference is not seen as drastically in the current research with those rollups being resolved. The results still have a decent amount of variation between these two results this is due to the grid resolution recorded by [15] which has a total resolution of 396 million carrying a significantly higher resolution compared to the current simulation of 35 million.

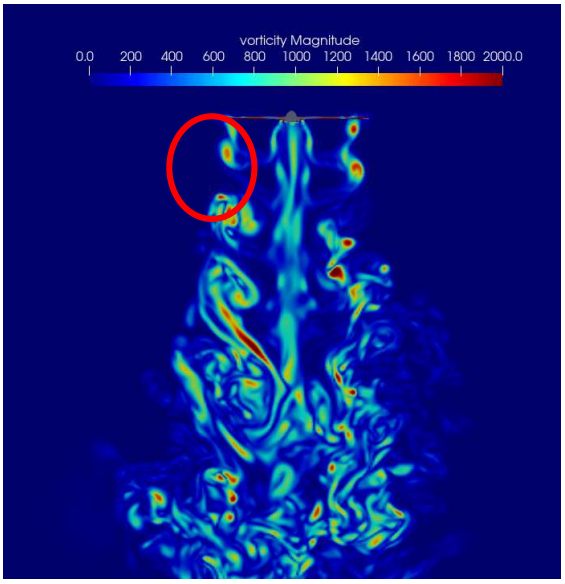

Figure 3.3 Vorticity Plot Z view

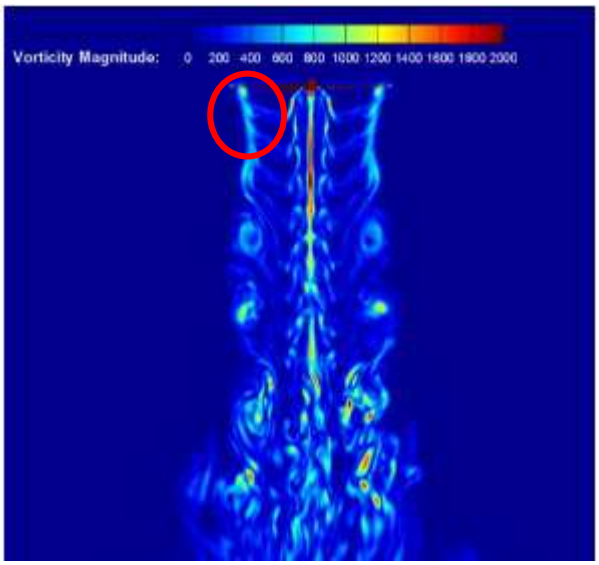

Figure 3.4 Vorticity plot Afari [2]

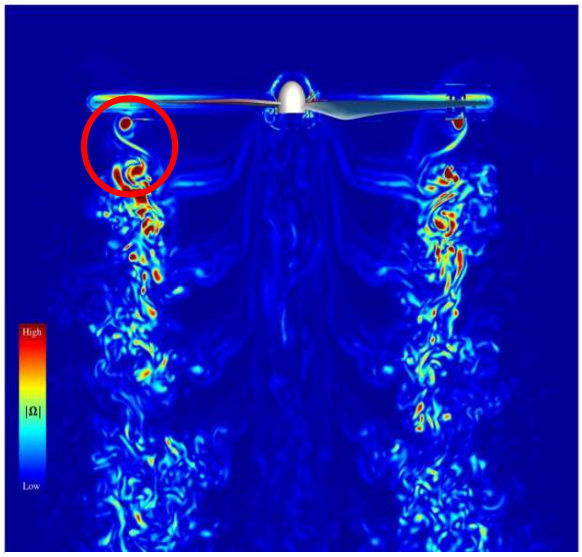

Figure 3.5 Vorticity plot [15]

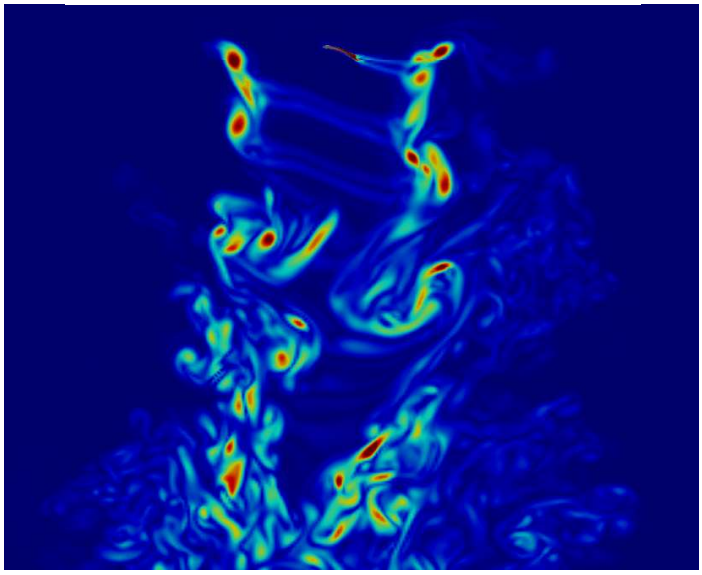

Figure 3.6 Vorticity plot X view

Figure 3.7 and Figure 3.8 are visualizations of the rotor from the x direction. There is an area of low velocity focused in front of the leading edge of the wing. Followed by an area of high velocity following the propeller. The demonstrate the visual pressure results of the simulation. Included in this visualization are 2 polar plots including an entire revolution of the propeller with 167 slices

taken along the midplane of the rotor and plotted. The results are shown for the top of the propeller which is an area of lower pressure for the rotor. After the slices are extracted the data is then postprocessed using MATLAB and plotted. The tip of the propeller is seen at the blue gradient where as outside of that mixing occurs between the high and low pressure.

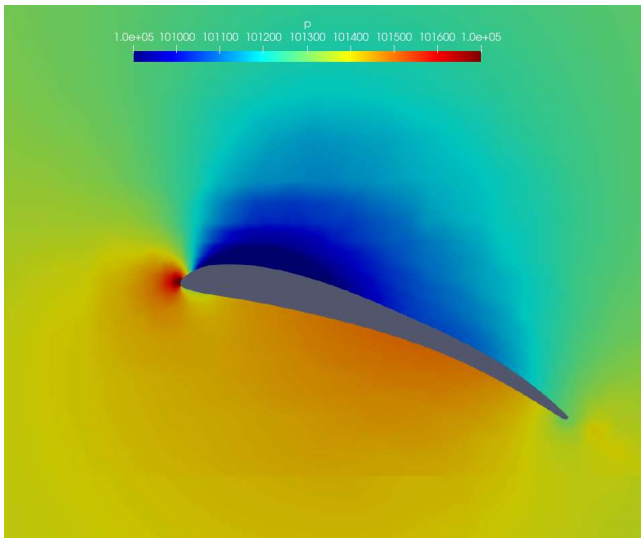

Figure 3.7 Pressure Plot X view

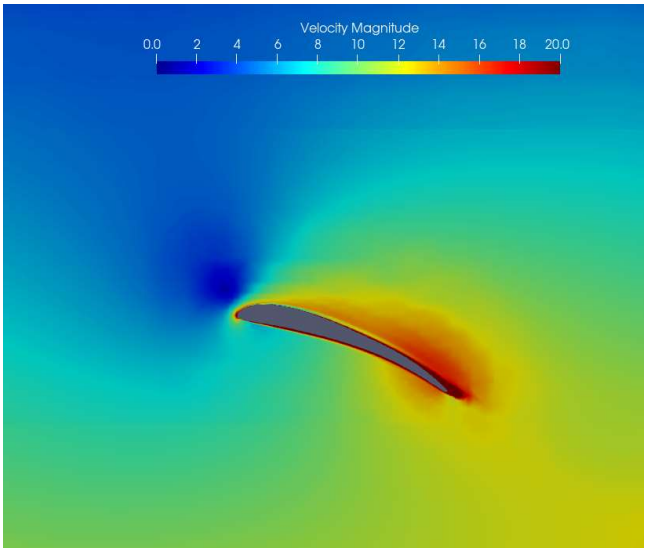

Figure 3.8 Velocity plot X view

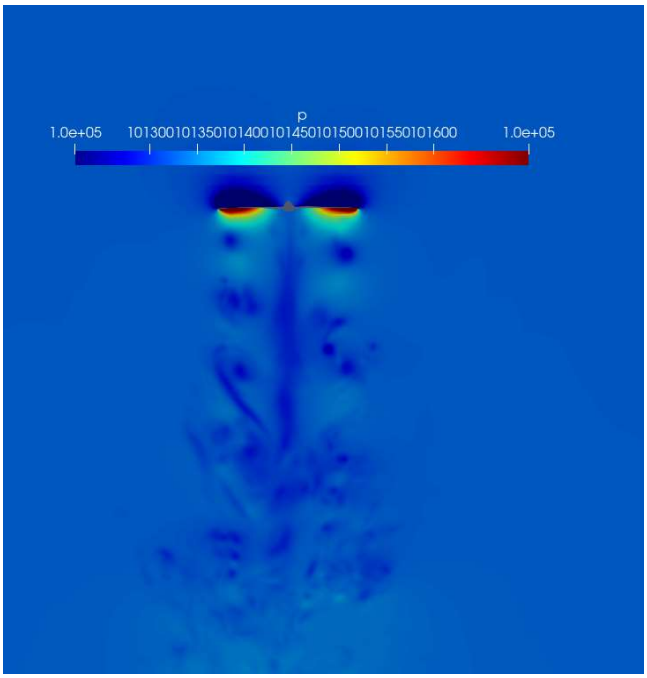

Figure 3.9 Pressure Results Z view Isolated propeller

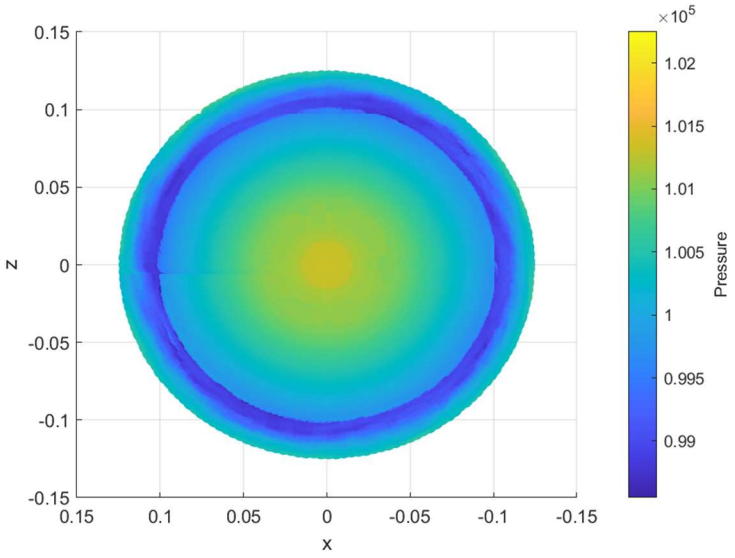

Figure 3.10 Pressure distribution Polar Plot (leading edge)

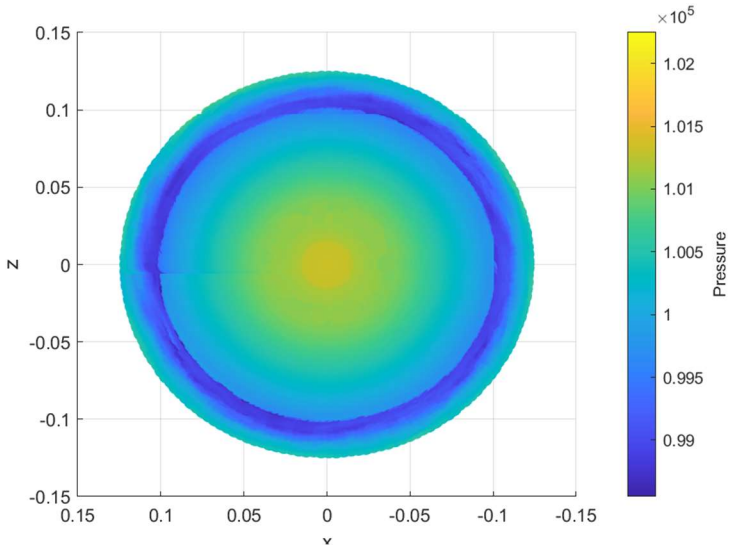

Figure 3.11 Pressure distribution Polar Plot (Trailing edge)

Form the polar plots an area of low pressure can be seen around the edges of the propeller this is reversed depending on the section of the propeller taken. Demonstrating the distribution of pressure throughout the rotor rotation. The isolated propellor needs to be evaluated numerically as well. To evaluate numerical data. A time averaged force plot of the data was conducted using the data taken from OpenFOAM and averaged using a user wrote program on MATLAB. The visual data is compared against Afari but the numeric data is mainly compared to the experiment conducted at Embry-Riddle Aeronautical University by Deters [24].

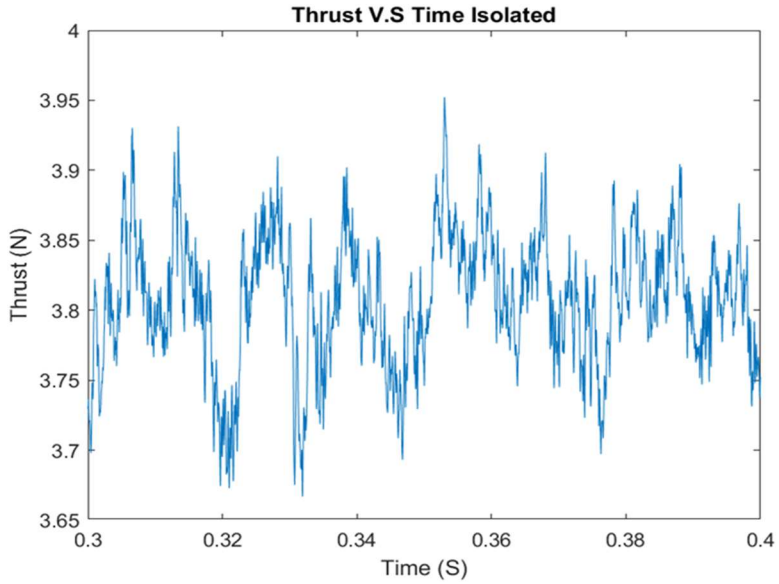

Figure 3.12 Thrust V.S Time Isolated Porpeller

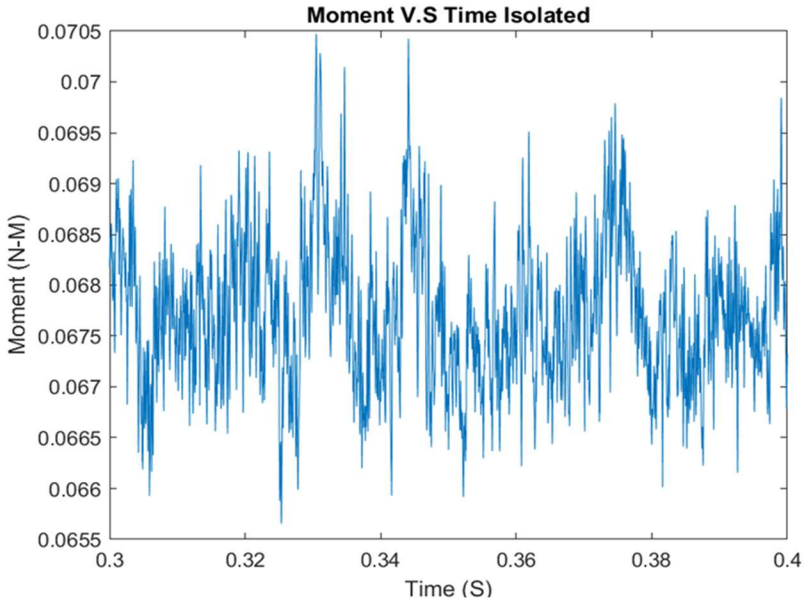

Figure 3.13 Moment V.S Time Isolated Propeller

Table 3.1 Thrust Comparison Isolated Rotor with [24]

Thrust (expiremental) N	Thrust (CFD) N	Thrust (Check) N	C_t (experimental) N	C_t (CFD) N	Error (%)	Error Check	F.O.M (isolated)	F.O.M (Check)
4.016	3.8073	3.585	0.0130	0.0128	5.133	7.02	0.5219	0.4860

3.2 Homogenous Ground Effects

The subsequent experiment conducted was the ground-only scenario, utilizing a mesh comprising 70 million cells and requiring approximately 12 hours of computational time per revolution on the NASA cluster. A total of 30 revolutions were simulated for this homogeneous case. The primary objective of this experiment was to simulate the rotor in hover directly above the building surface. This setup enables a comprehensive examination of the process of hovering a VTOL craft above a rooftop. The results of this experiment are depicted below.

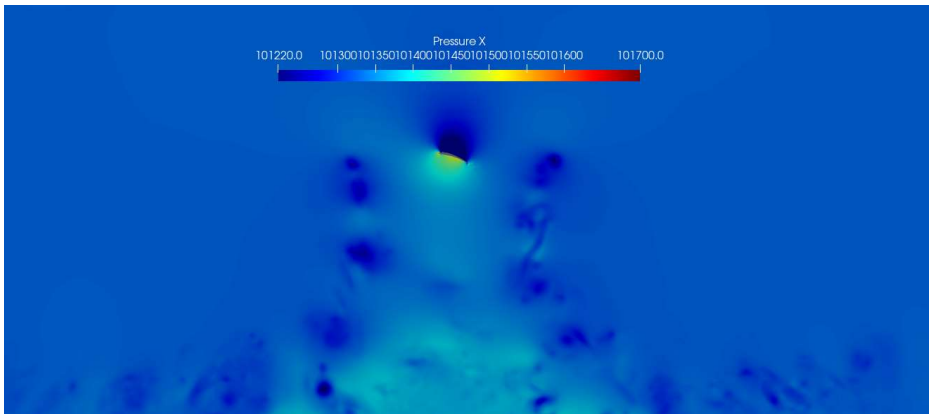

Figure 3.14 Pressure x View Homogeneous Ground Effect

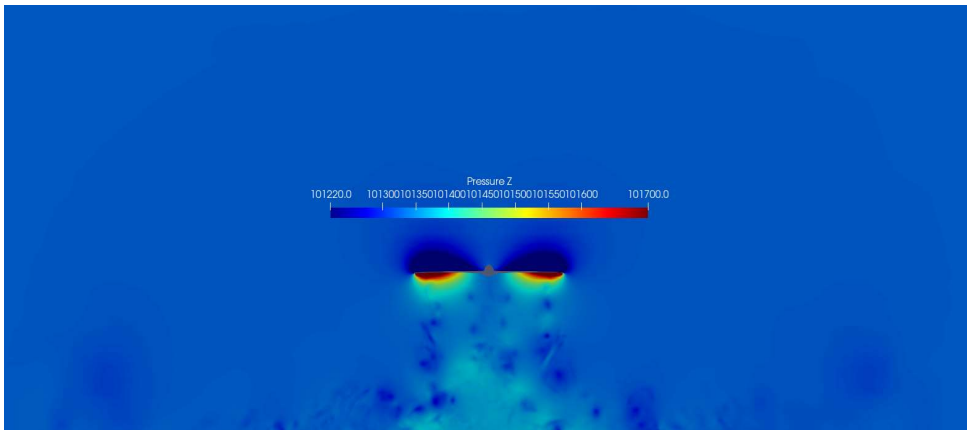

Figure 3.15 Pressure Z view Homogeneous Ground Effects

The pressure results yield intriguing visual data, revealing a high-pressure influx directly beneath the propeller, with low-pressure zones surrounding the propeller. Moreover, the velocity profiles exhibit a notable characteristic resembling the fountain flow observed in the research conducted by Mora [25]. Their findings are presented below for comparison.

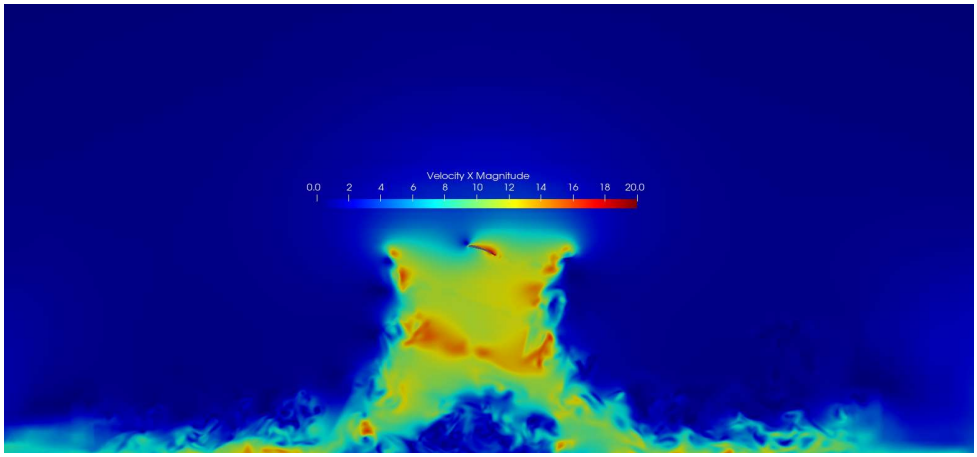

Figure 3.16 Velocity X View Homogeneous Ground Effect

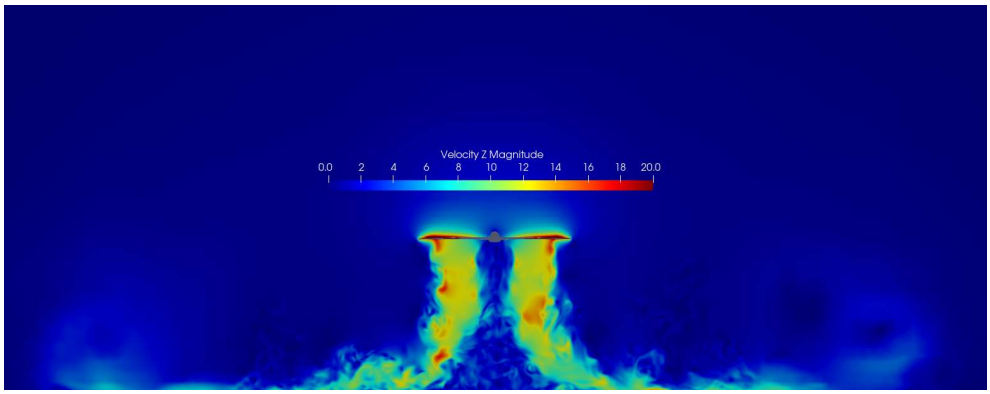

Figure 3.17 Velocity Z View Homogeneous Ground Effect

These results visually represent one another very well and it can be seen that at the 1.25D distance away from the ground the flow fields nearly match with the exception of the mixing going on in the current simulation. This is due to the difference in resolution with the fine mesh allowing for better visualization of the fountain flow.

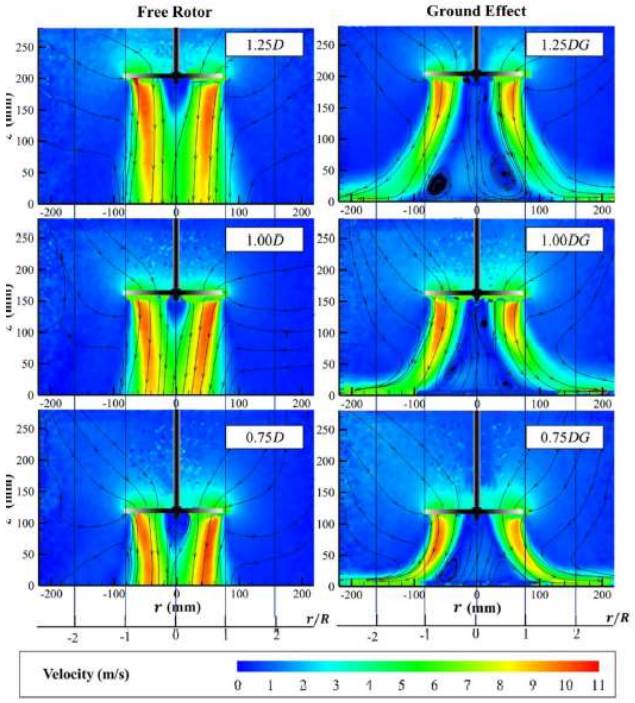

Figure 3.18 Velocity Profiles at Different Heights Mora [25]

It's crucial to compare the values obtained from the isolated rotor simulation with those incorporating ground effect interactions. The table below illustrates that while there is a marginal increase in thrust output with ground effect, the observed increase is notably less than anticipated. This discrepancy in results may be attributed to the separation distance between the rotor and the ground.

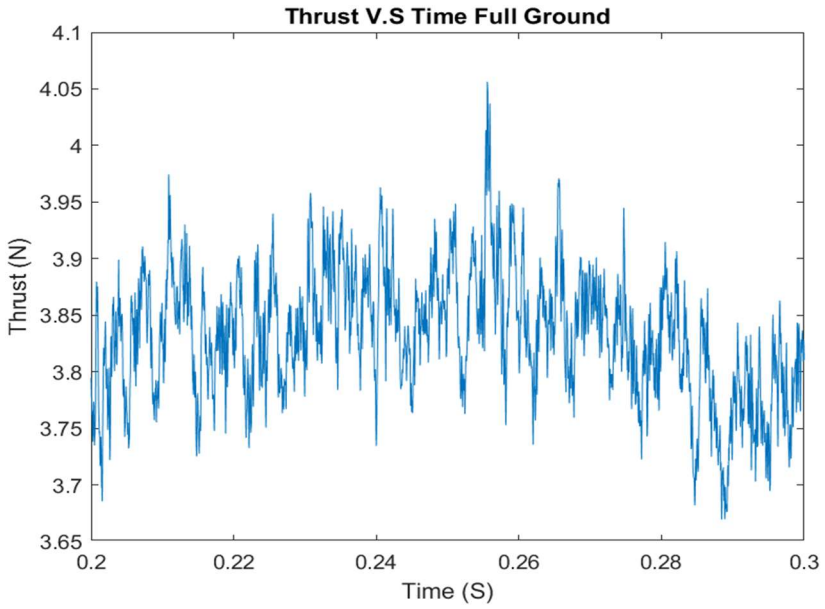

Figure 3.19 Thrust V.S Time Full Ground

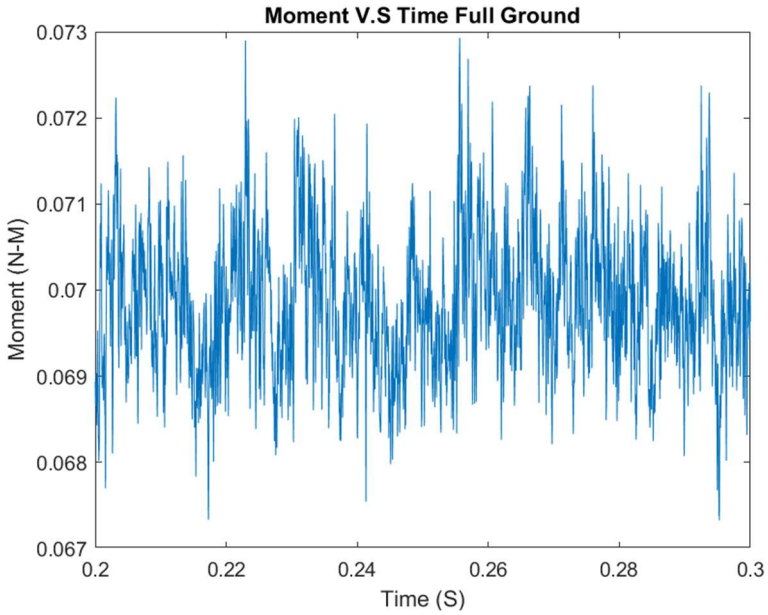

Figure 3.20 Moment V.S Time Full Ground

Table 3.2 Thrust Ground Effects Compared to Isolated Rotor

Thrust (Isolated) N	*Thrust (Full Ground) N*	*Thrust (Check) N*	*C_t (Isolated)*	*C_t (Ground)*	*C_t (Check)*	*Percent Change (%)*	*Percent Change (Check)*	*F.O.M (Full Ground)*	*F.O.M (Check)*
4.016	*3.8073*	*3.6132*	*0.0128*	*0.0128*	*0.0115*	*5.133*	*5.37*	*0.5202*	*0.4909*

The resulting difference in these numbers is less than 5 percent which is not a significant enough change to notice. A change like this could be due to the measuring window taken and may not be physical.

3.3 Non-Homogeneous Ground Effects

Finally, a partial ground effects test case was conducted. The rotor is intended to simulate a craft approaching the landing zone of the building directly centered on the edgewise span of the building this along with the full ground effects case helps understand and quantify the Urban

environment better as a whole allowing there to be more understanding. Initially velocity magnitude in both the X and Z direction is shown.

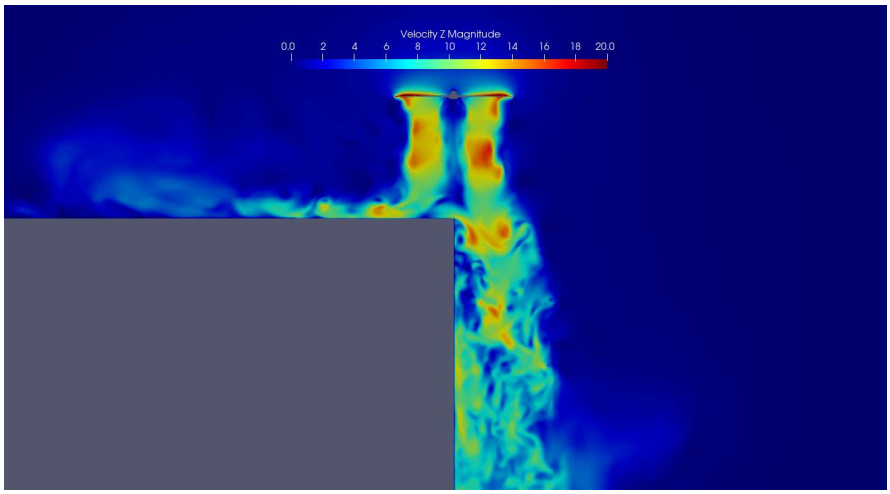

Figure 3.21 Velocity Z Partial Ground Effects

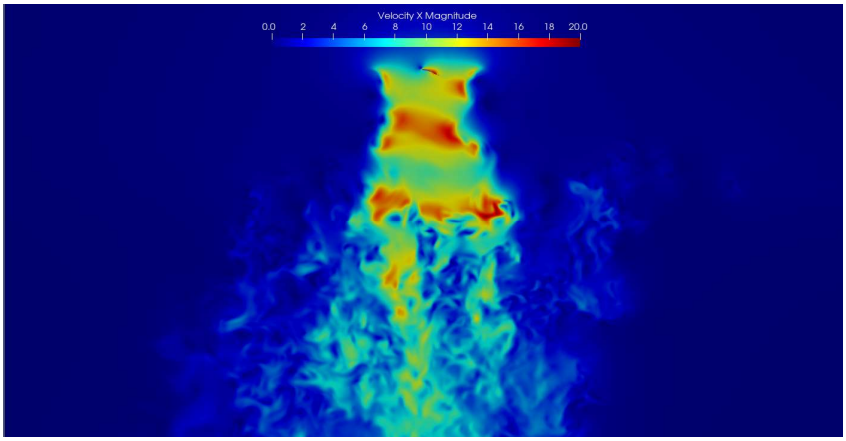

Figure 3.22 Velocity X Partial Ground Effects

The velocity profile especially with respect to the Z plane provides very interesting insight into the way flow develops in a non-homogeneous field. The bottom of the velocity profile shows a spool up with an area of low velocity located at the center of the profile and areas of higher velocity

located around the edges. It's also important to note as has been previously stated that the no-slip boundary condition causes the flow to become zero at the wall. This seems to result in the flow interacting beneath the rotor. These results are what is to be expected and are shown by [25] as is seen below.

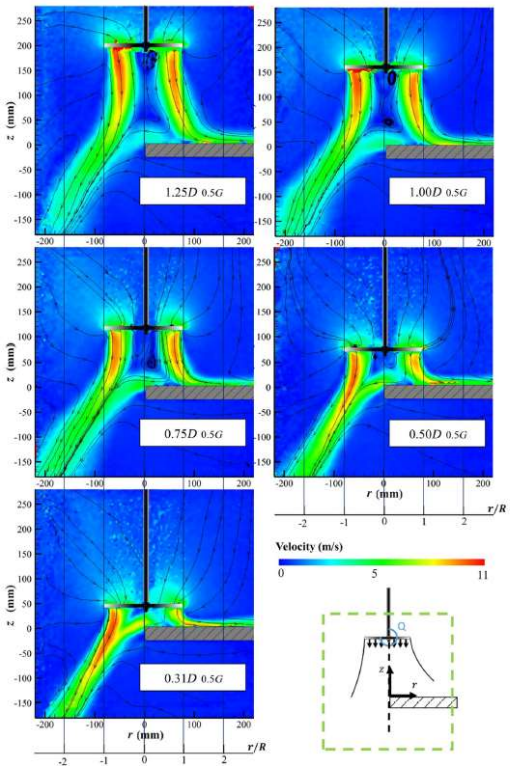

Figure 3.23 Partial Ground Effects at Different Heights Mora [25]

Similar to the homogeneous case, the velocity profiles exhibit a close match with each other, providing evidence of the overall validity of the mesh. This alignment is particularly evident when compared to the Figure 3.23 in the top left, which is also centered around the midplane and positioned at the same distance. Additionally, the velocity spool-up is depicted.

It's important to note that the wall does not extend to the end of the simulation domain, which explains why the open side of the rotor does not exhibit flow detachment from the wall, as observed

in the current simulation. Furthermore, due to the higher rotational speed of the rotor in comparison to the experiment, there is a greater likelihood of flow separation. The vorticity plots are depicted below for further examination.

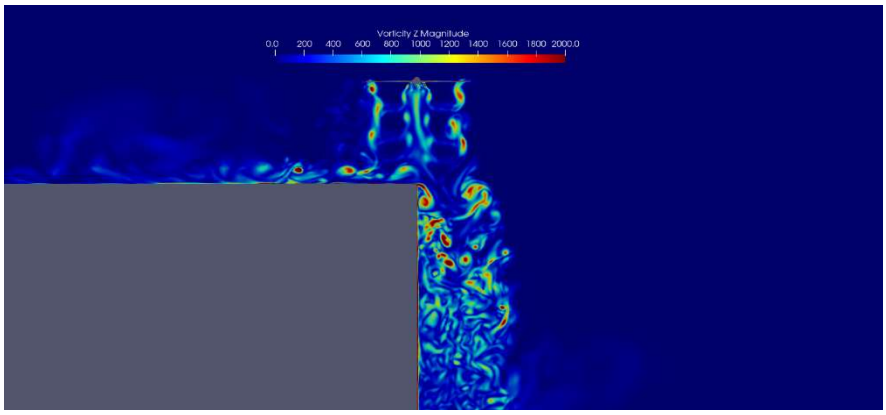

Figure 3.24 Vorticity Z Partial Ground Effects

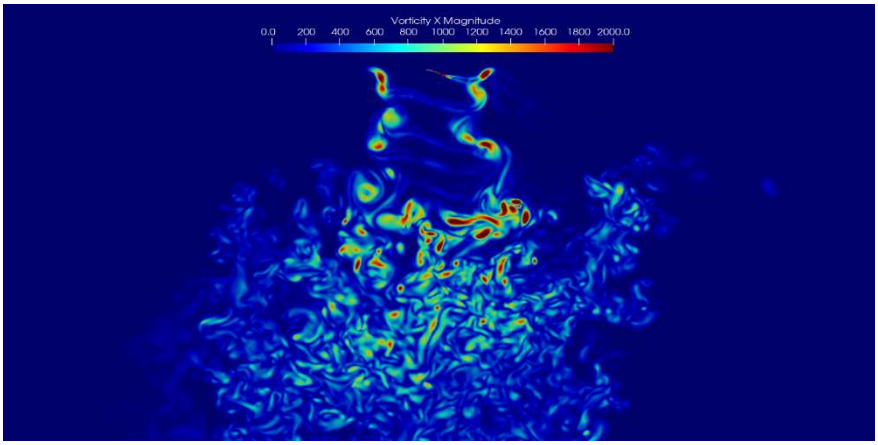

Figure 3.25 Vorticity X Partial Ground Effects

The vorticity plots demonstrate similar characteristics as the velocity plots with a notable similarity at the corner of the wall showing the spool up around the edge of the building. The Z cut is taken along the center of the rotor as is the X cut. Below the pressure profiles are shown.

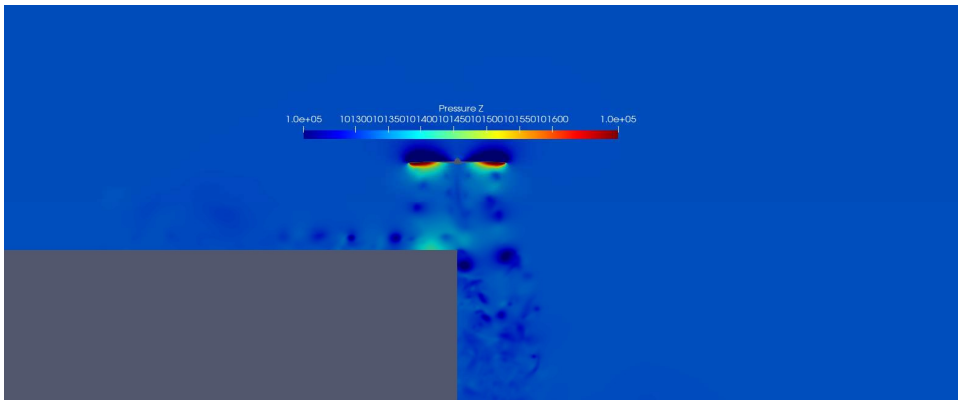

Figure 3.26 Pressure Z Partial Ground Effects

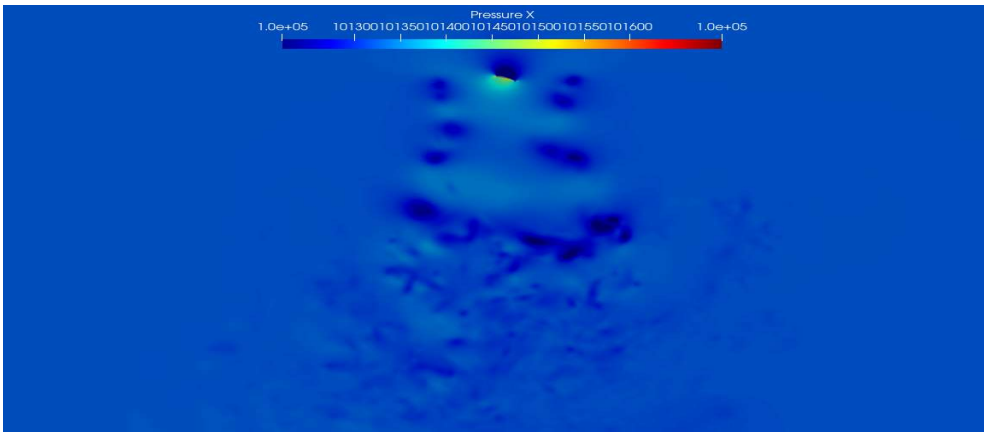

Figure 3.27 Pressure X Partial Ground Effects

The pressure profiles demonstrate a pressure spike around the corner of the building this pressure spike is around 101400 pascals which is significantly greater than the low-pressure region which has a value of 101200 pascals around a 200-pascal jump. Due the edge of the building

causing interaction. The pressure data is a very significant data source from the simulations as it demonstrates the force off the propellor. This gives the validity to the results showing that the mesh has been generated correctly. The resulting force data from the non-homogeneous propellor is shown.

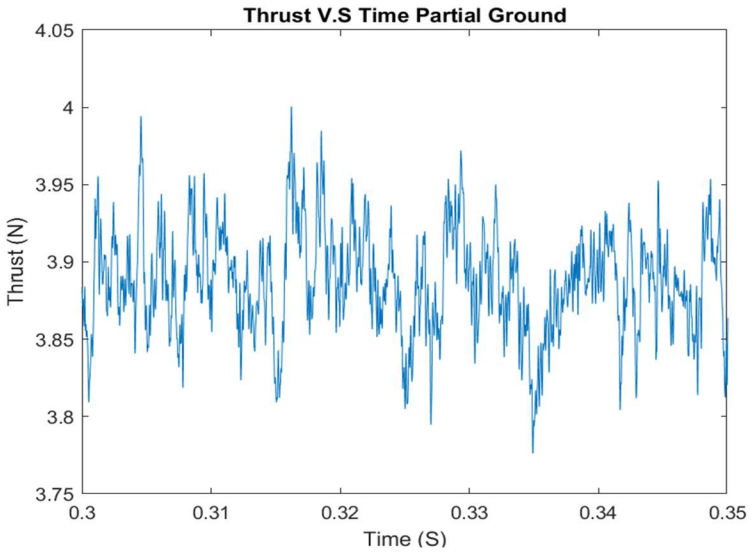

Figure 3-28 Total Force V.S Time Partial Ground

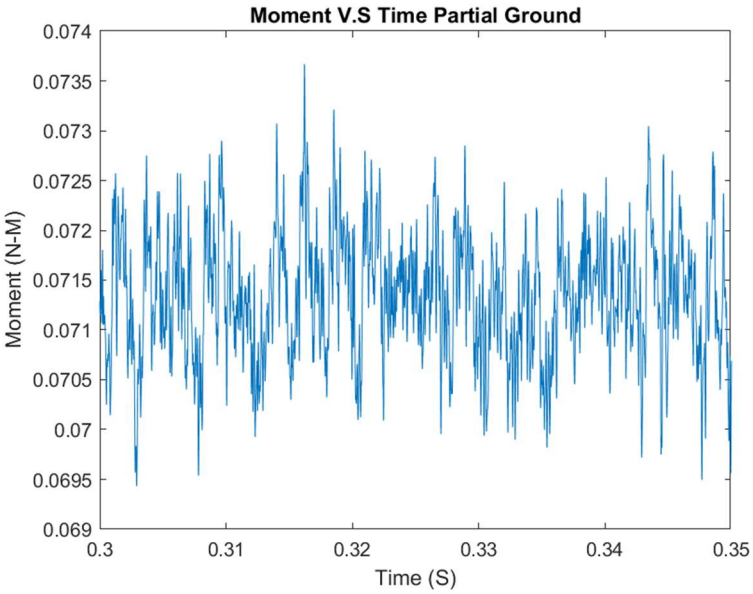

Figure 3-29 Total Force V.S Time Partial Ground

Table 3.3 Thrust Data for Partial Ground Effects

Thrust (Isolated) N	Thrust (Partial Ground) N	Thrust (check) N	C_t (Isolated) N	C_t (Partial Ground) N	C_t (check) N	Percent Change (%)	F.O.M (Par Ground)	F.O.M (Check)
3.81	3.89	3.5853	0.0128	0.0121	0.0114	2.01	0.5102	0.4860

There is a relatively low change in thrust in all of the varying simulations with the largest disparity showing a change of only 3%. The F.O.M demonstrates the best performance related to the isolated rotors. These results follow expected performance trends. With the propeller having to put more "work" in to generate a similar thrust causing the moment to increase. This shows that the best performance for the rotor is when there is no surface below the rotor. Which is understandable given the fact that the ground is going require more energy for the thrust. This is why helicopters require a higher rpm for takeoff.

There is however a large source of concern in regards to the full ground interaction. According to the rotorcraft Textbook by Leishman [37] the rotorcraft should see an increase in full ground effects and less of an effect in partial effects. This is apparent in the Thrust. This is an issue in the new mesh with the partial ground effects demonstrating an increase in Thrust greater than that of the full ground. However also included in this work when the separation distance gets as far away as the current run is the change in thrust is minute less than 5% which is clearly demonstrated by all meshes.

4 Acoustics

The other primary focus of this research along with evaluating the performance of the propellor is the acoustic effects of the propellor as the downwash interacts with the walls. The effects studied and recorded here are near field acoustics. These acoustic effects are discovered using 3 pressure probes that have been placed throughout the mesh bound within the meshing region. These probes collect the data at these locations and output the results. The results are then plotted against time. These results are compared against one another and against the results from Afari [2]. The results are near field acoustics. Along with these values collected from the implemented FWH surfaces are used. These surfaces have their own unique challenges. Mainly focused on the generation of the surfaces. The surfaces are treated such that the flow passes through, and data is collected at these points. These simulations where ran for an additional 10-time steps and acoustic data was collected over this time. The previously generated geometry does not allow for the appropriate data collection for acoustics. This is due to the scheme chosen which causes damping of the collected pressure wave causing the results to be unreliable. The check mesh is then used for probe data collection.

4.1 Acoustic Data Collection

The pressure probe data is located at three points throughout the simulation these locations are demonstrated in Figure 4.1. These acoustic collection points vary for the appropriate geometry. If the probe location is too close to the ground, there will be a large number of reflections. These reflections cause the prediction of noise to not be accurate, so an in-plane probe location and a location slightly above plane is chosen for the full building. There are also a probe location chosen behind the probe. For the half building due to the one side not having ground reflections it is possible to incorporate the full spectrum of probe locations. This allows for better comparison between the two values. The original mesh acoustic prediction along with the partial acoustic prediction is shown in the following sections. The locations are shown below and loosely

demonstrated in Figure 4.1, Figure 4.2, and Figure 4.3. There are also locations in the Z direction not shown. This is used for near field acoustic prediction. The in-plane location and the below plane locations are the same for both runs compared.

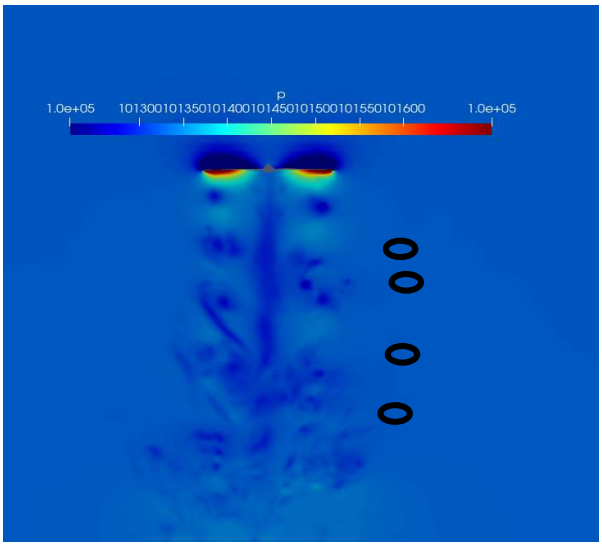

Figure 4.1 Probe locations for Near Field Acoustic Collection

Table 4.1 Probe locations Isolated Rotor

Location (deg)	X	Y	Z	Radius
Probe (0)	-0.5975	0	0	0.5975
Probe (22. 5)	-0.552018	0.228653	0	0.5975
Probe (-22.5)	-0.552018	-0.228653	0	0.5975
Probe (45)	-0.422496	-0.422496	0	0.5975
Probe (67 Z)	0	0.228653	0.552018	0.5975
Probe (0)	0	0	0.5975	0.5975

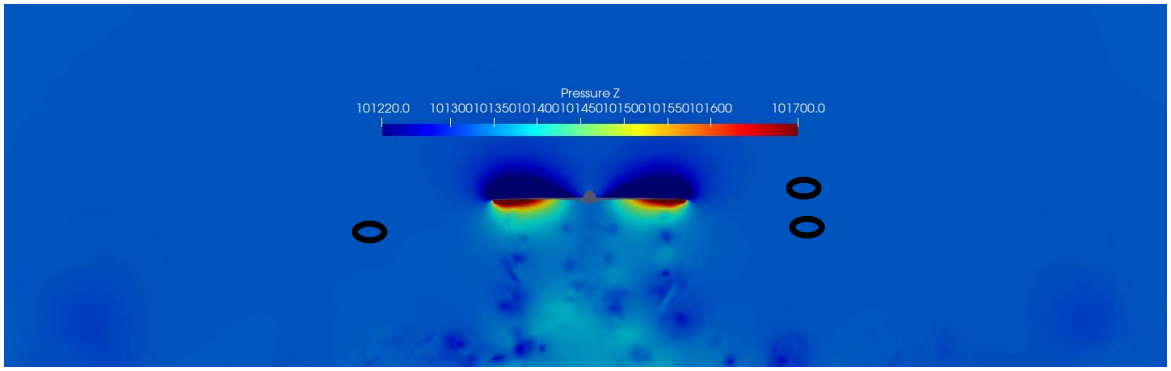

Figure 4.2 Approx. Probe Locations Full Ground

Table 4.2 Probe Locations Full Ground

Location (deg)	X	Y	Z	Radius
Probe (0)	-0.5975	0	0	0.5975
Probe (−22.5)	-0.552018	0.228653	0	0.5975
Probe (180)	0.5975	0	0	0.5975
Probe (67.5 Z)	0	0.228653	0.552018	0.5975

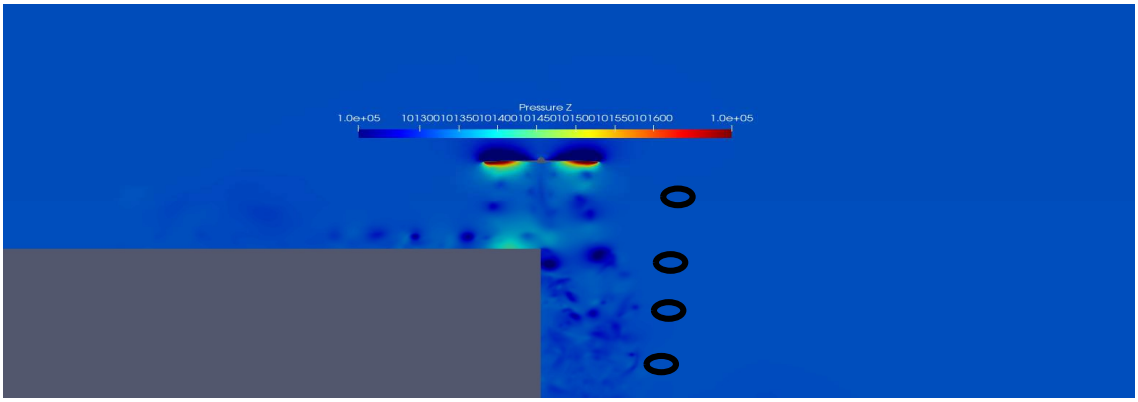

Figure 4.3 Approx. Probe Locations Partial Ground

Table 4.3 Probe locations Partial Ground

Location (deg)	X	Y	Z	Radius
Probe (0)	-0.5975	0	0	0.5975
Probe (22. 5)	-0.552018	0.228653	0	0.5975
Probe (-22.5)	-0.552018	-0.228653	0	0.5975
Probe (45)	-0.422496	-0.422496	0	0.5975
Probe (67 Z)	0	0.228653	0.552018	0.5975
Probe (0)	0	0	0.5975	0.5975

4.2 Isolated Rotor Acoustics

As discussed, earlier probe data is taken along points in the simulation this data is then plotted against time for one revolution. This pressure data can be seen below for the fluctuation during a full blade passing. The pressure fluctuates as the blade passes along and we can see a very similar trend in the pressure fluctuation as the bade passes for each probe location.

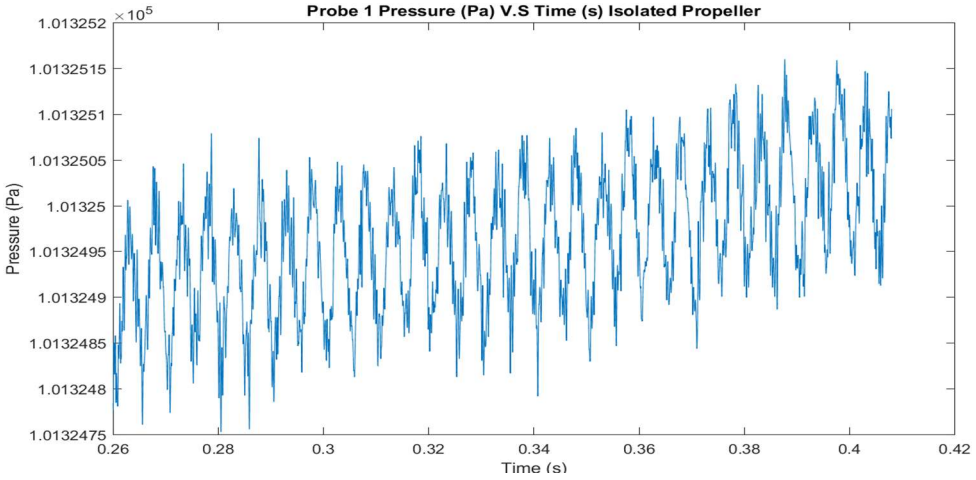

Figure 4.4 Probe Pressure Data V.S Time Isolated Rotor for First Probe Location

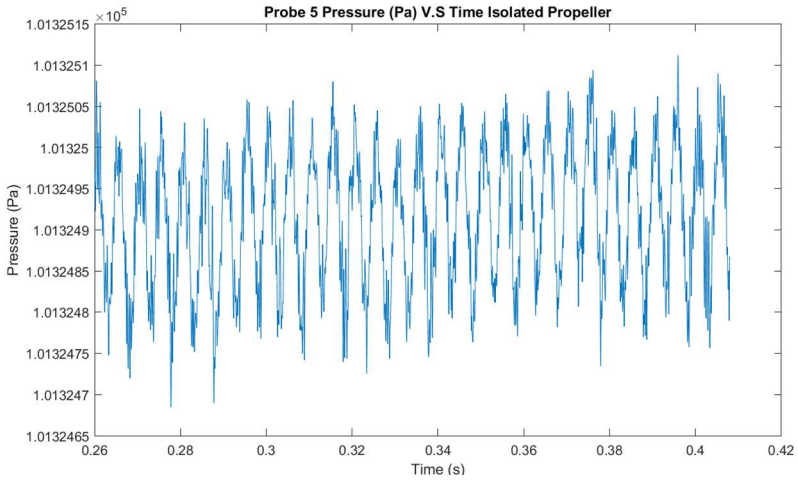

Figure 4.5 Probe Pressure Data V.S Time Isolated Rotor for Second Probe Location

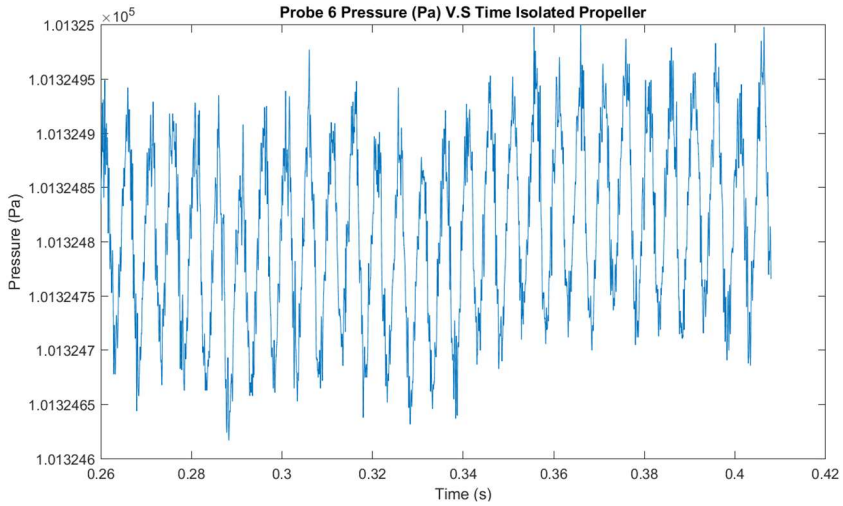

Figure 4.6 Probe Pressure Data V.S Time Isolated Rotor for Third Probe Location

The given pressure data represents the convergence of the pressure. These are plots of the last 10 rotations of the probe when acoustic collection began. Using a code developed at Embry-Riddle the sound level can be calculated. These plots for the isolated rotor can be compared with work completed Afari [2]. The isolated results will be compared with both the partial and entire ground results. Only the acoustic check mesh was used for acoustic data collection.

The Sound Pressure level is calculated using the probe data at different frequencies. It important to note that the data presented is for near field and not far. This results in larger pressure differences and an overall larger pressure level. The maximum sound experienced is around 60 dB for all cases this compares very closely to [16] there is slightly higher acoustic prediction but this is to be expected because of the change with respect to the rotor used the rotor used by [16] is slightly underperforming and thus generated less noise but at the cost of lower. Figure 4.7 shown by Afari [16] is from a study done on multirotor interactions. These interactions are not important for this paper, but the blue line is of importance. This relation shows the pressure fluctuation as well as the values demonstrated by Afari [16] although are lower in magnitude follow a really similar pressure fluctuation trend. Its important to note that the fluctuation of noise here is more important than the values because the technique done to record the acoustic values are different with these values being Far-field and not near field values. This cause a large change in the value of the noise because the location the noise is taken from is very different.

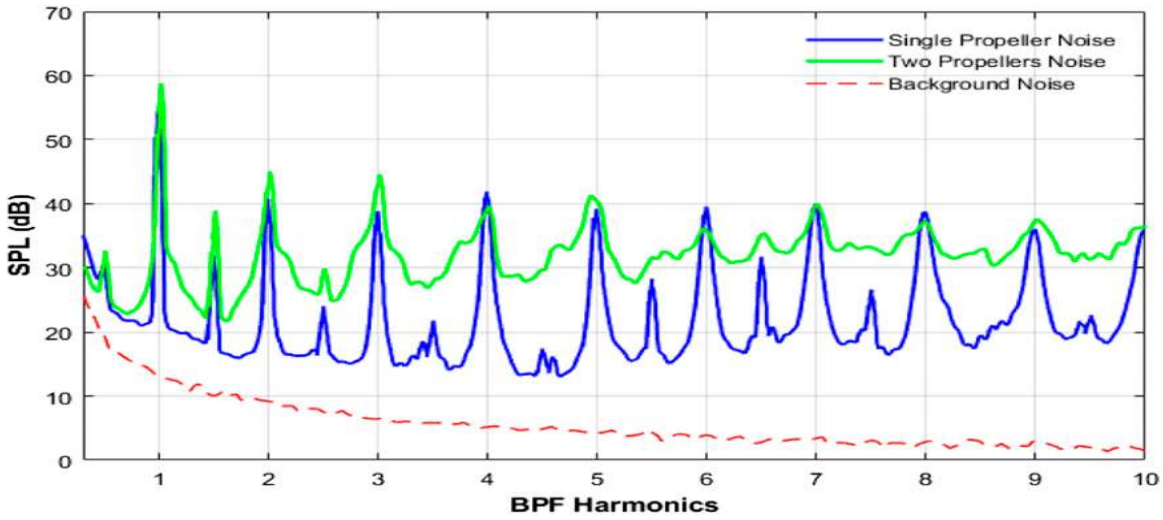

Figure 4.7 Sound Pressure Level Isolated Rotor and Multi Rotor V.S BPF Harmonics Afari [16]

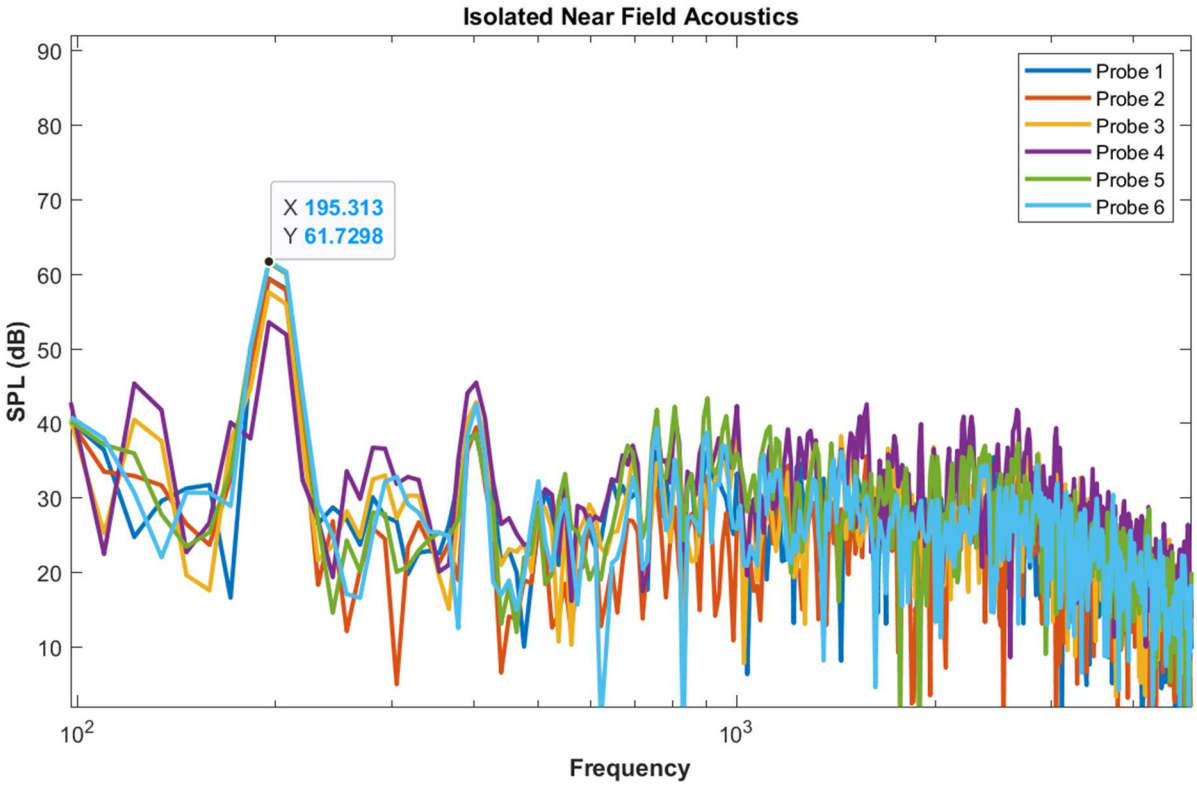

Figure 4.8 Sound Pressure Level V.S Frequency Isolated Rotor

These values are not different in amplitude due to the distance that the noise was measured and the trends are very similar with Afari [16] recording a difference in decibels between 10 and 20 peak fluctuations. The current rotor however is noisy if the user is standing in a close proximity. Sound levels for the human ear are demonstrated below in the figure with the noise generated by this blade being as loud as a large conversation or a city car traffic. Next Partial and full ground effects are to be evaluated.

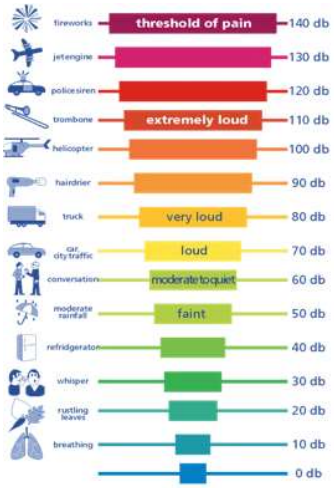

Figure 4.9 Noise Levels for Real World Applications [33]

4.3 Homogeneous Ground Acoustics

Full ground effects the prediction of noise in the ground portion follows the identical process of the isolated rotor with the same probe locations and the same process to evaluate spectral level. The Pressure probe data and the SPL sound level are shown below.

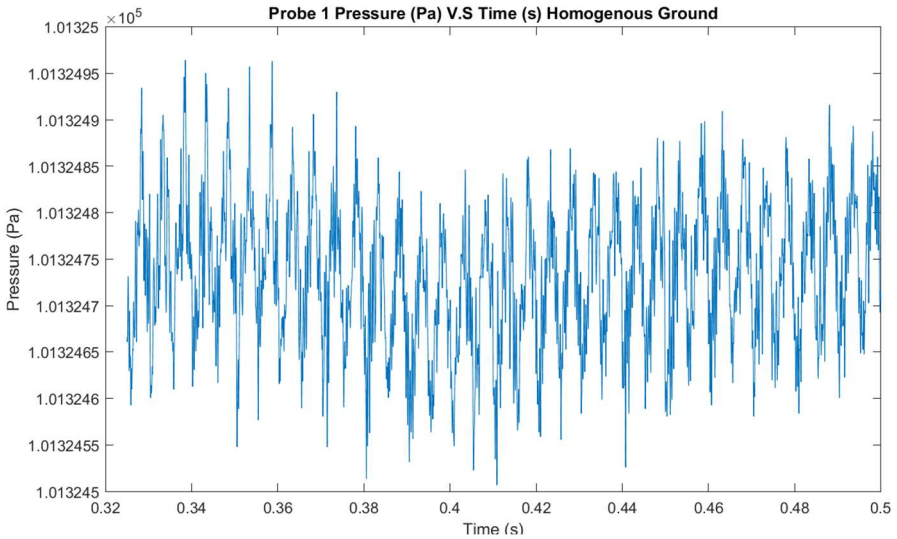

Figure 4.10 Probe Pressure Data V.S Time Full Ground Effects Rotor for First Probe Location

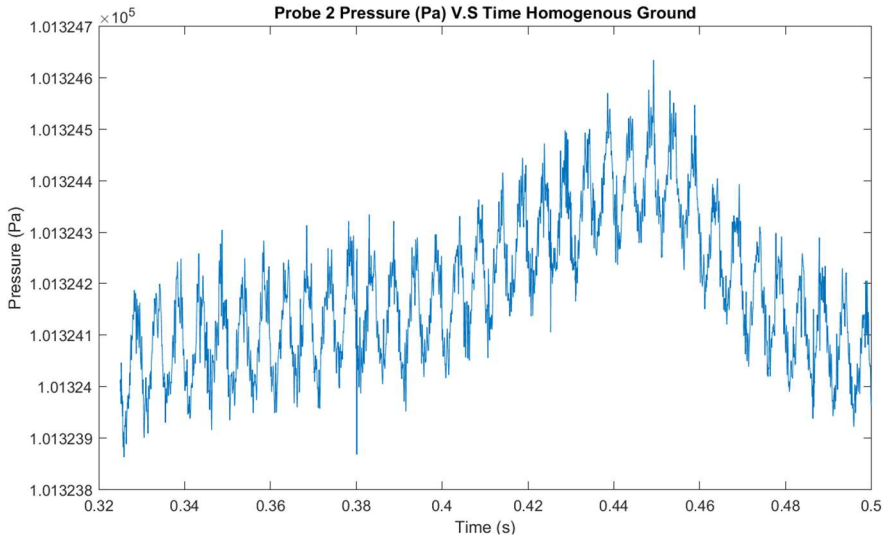

Figure 4.11 Probe Pressure Data V.S Time Full Ground Effects Rotor for Second Probe Location

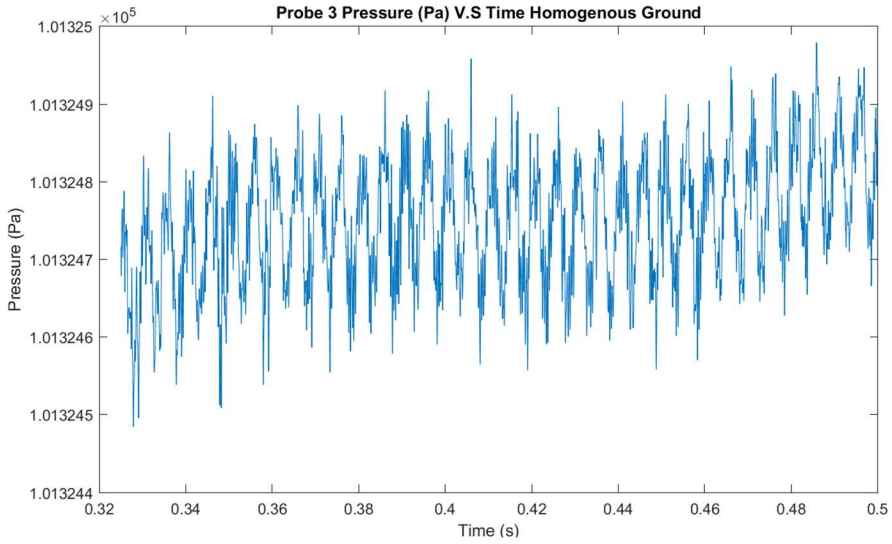

Figure 4.12 Probe Pressure Data V.S Time Full Ground Effects Rotor for Third Probe Location

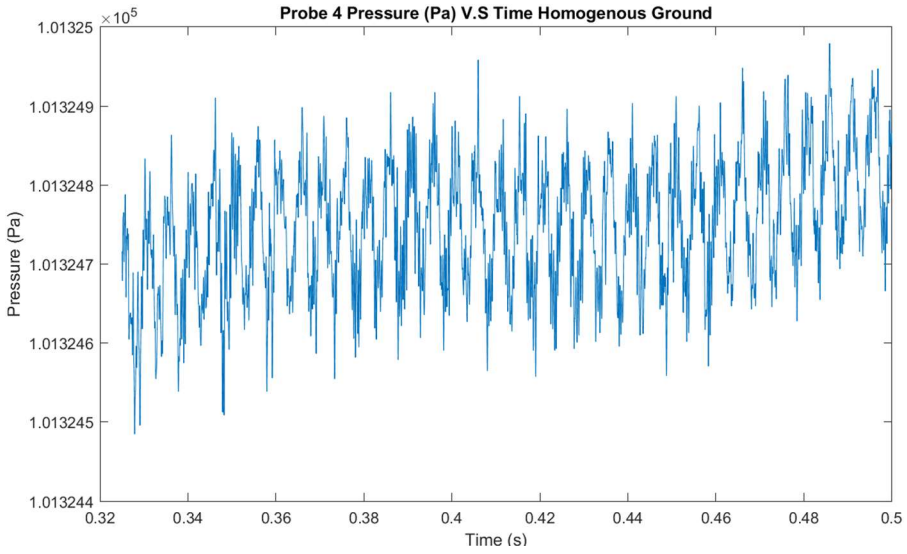

Figure 4.13 Pressure probe Data

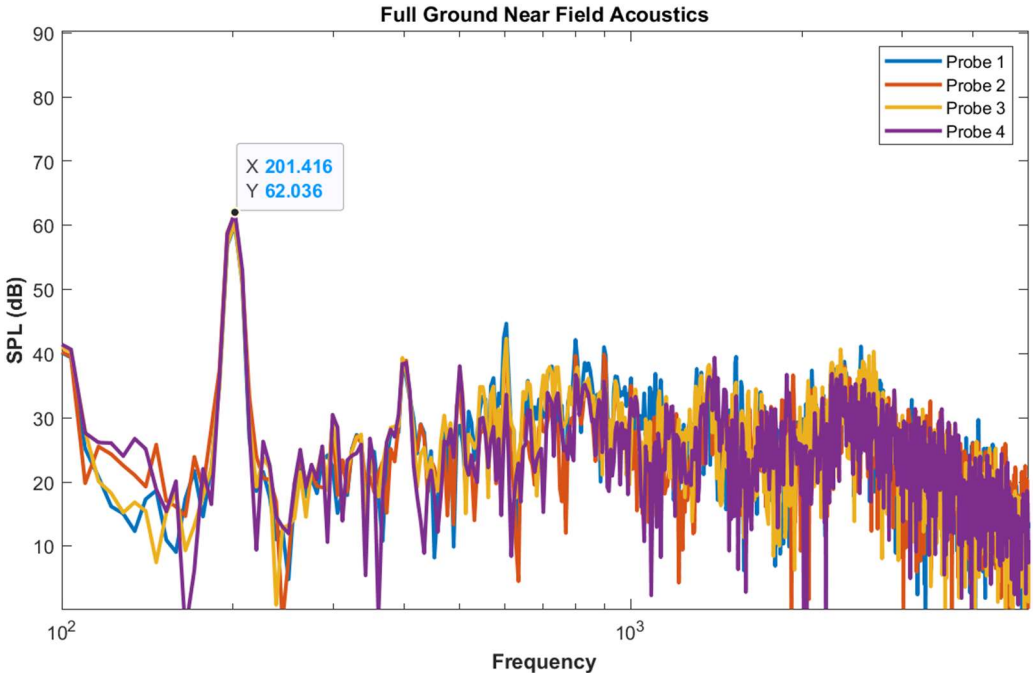

Figure 4.14 Sound Pressure Level V.S Frequency Ground Effects Rotor

The reason that there less probe locations is because from prior testing if a lower probe location is used a large error source for the probe in the near field appears this seems to be an issue with the

location of the third probe. If a lower probe is located very close to the ground source as seen by the below figure. This causes a large amount of ground reflections and an area of high pressure around this probe point demonstrating that the pressure data here is most likely not a fantastic point for measuring the data for the Full-Ground effects unlike the data for the isolated rotor and the data for the partial ground effects which are shown below these probe locations are not located close enough to the surface to generate an immediate pressure reflection. This was a main reason for the new check mesh.

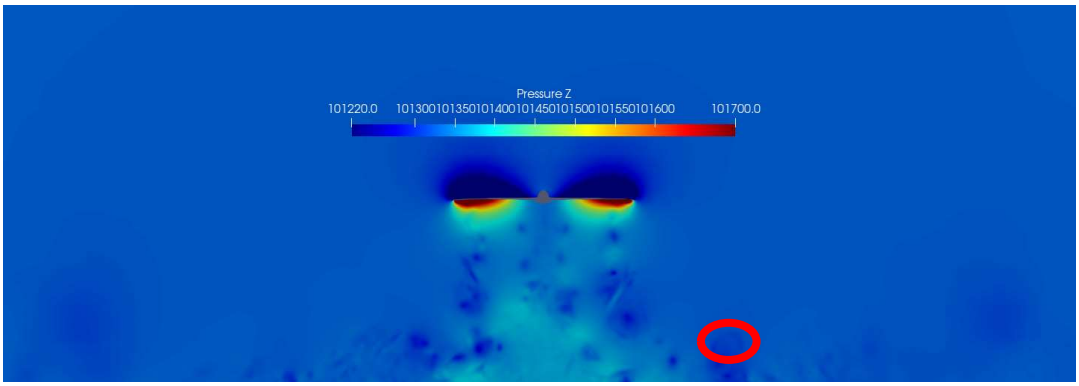

Figure 4.15 Near Field Full Ground lower probe location

4.4 Non-Homogeneous Ground Acoustics

Finally for Partial ground effects the same process is followed as the isolated rotor and full ground. The probe locations are the same as is the approach to determining the sound level emitted from the propeller. The following data demonstrates the results from the partial ground propeller. The pressure probe data follows the same convergence as demonstrated by the prior results the Partial ground near field acoustic results is shown below.

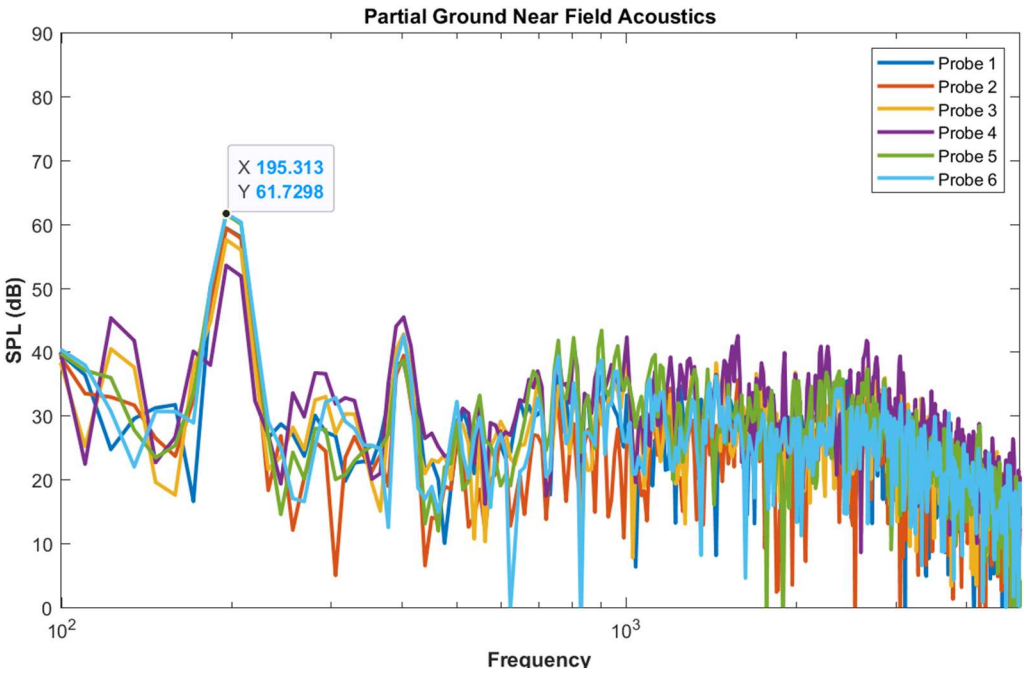

Figure 4.16 Sound Pressure Level V.S Frequency Partial Ground Effects Rotor

This partial ground data shows close comparison with all probe values showing an increase in the noise as the probe location gets closer to the ground values. This shows that the inclusion of the ground provides a decibel increase in near field noise. Noise values for all three runs are compared in the table below. The probe of interest is the lower probes which demonstrate the noise levels closest to the ground surface. The only probes valid for comparison are the ones in plane and slightly above plane as compared in the following table.

Table 4.4 Upstream Probe Noise Level Comparison

Probe Noise Comparison Highest Noise	
Isolated (dB)	61.7
Homogeneous Ground (dB)	62.036
Non-Homogeneous Ground (dB)	61.75

The implementation of the ground demonstrates a partial increase in the noise but does not demonstrate a large increase in decibels. This increase is less than 3% and results in a very minor change. From this it can be concluded that the pressure does not see a large increase however further development in FWH surfaces needs to be implemented in order to ensure accurate acoustics are demonstrated and calculated.

4.5 Far Field Noise

Also, during this time sampling surfaces where implemented. These FWH surfaces have a surrounding cylinder to collect data at 2.5 radii away as well as end caps with a certain spacing constraint. This spacing constraint allows the data to be collected at the various noise portions. These Surfaces for the isolated rotor are shown below. For the ground effect case the surfaces are almost identical just smaller. As for the partial ground effect case a different approach needs to be taken to ensure appropriate collection of data is conducted. This formulation is used for Far Field Noise prediction. Far field Noise has a unique challenge. This includes implementing a surface surrounding the region of the blade that can capture far field acoustics. Far Field acoustics are of high importance in aeroacoustics and provide a large amount of interest many different approaches

are taken to resolve this complex issue as discussed by Afari [2] but for the interest of this research the implementation of Williams & Hawkings [31]. The formulation is simplified below. Beginning with the continuity equation.

$$\frac{\partial}{\partial t}\int_v \bar{\rho} dV = \frac{\partial}{\partial t}\int_{v1} \rho^1 dV + \frac{\partial}{\partial t}\int_{v2} \rho^2 dV \tag{4.1}$$

Then the equation is implemented into a moving surface discussed by [2] then the equation turns into:

$$\frac{\partial}{\partial t}\int_v \bar{\rho} dV = -\int_{\Sigma} (\overline{\rho u_l}) l_i d\Sigma + \int_s [\rho(u_i - v_i)]_1^2 n_i dS \tag{4.2}$$

Following this the divergence theorem is applied to equation 23. Then it is assumed that if an equation has a zero solution that defines a Surface so that if $f < 0\ in\ 1$ and $f > 0\ in\ 2$ the integration over S can be rewritten. This then simplifies into the generalized continuity equation.

$$\frac{\partial \bar{\rho}}{\partial t} + \frac{\partial}{\partial x_i}(\overline{\rho u_l}) = [\rho(u_i - v_i)]_1^2 \delta(f) \frac{\partial f}{dx_j} \tag{4.3}$$

Similarly, the momentum can be manipulated from its base form to obtain the final form [31]:

$$\left(\frac{\partial^2}{\partial t^2} - c^2 \frac{\partial^2}{\partial x_j}\right)(\overline{\rho - \rho_0}) = \frac{\partial}{\partial t}[\rho_0 U_n \delta(f)] - \frac{\partial}{\partial x_i}\left[L_{ij} n_j \delta(f)\right] + \frac{\partial^2 T_{ij}}{\partial x_i \partial x_j} \tag{4.4}$$

Next the Green function is utilized [2] when this equation is executed it gives the following form:

$$4\pi c^2(\rho-\rho_0)$$

$$=\frac{\partial}{\partial t}\int_s [\frac{\left[(\rho_0 u_n+(\rho-\rho_0)(u_n-v_n)\right)]}{r|1-M_r|}]ret\ dS$$

$$+\frac{1}{c}\frac{\partial}{\partial t}\int_S \left[\frac{P'_{ij}+\rho u_r(u_n-v_n)}{r|1-M_r|}\right]_{ret} dS$$

$$+\int_S \left[\frac{P'_{ij}+\rho u_r(u_n-v_n)}{r^2|1-M_r|}\right]_{ret} ds$$

$$+\frac{1}{c^2}\frac{\partial^2}{\partial t^2}\int_V \left[\frac{T_{rr}}{r|1-Mr|}\right]_{ret} dV+\frac{1}{c}\frac{\partial}{\partial t}\int_V \left[\frac{3T_{rr}-T_{ii}}{r^2|1-Mr|}\right]_{ret} dV+\int_V \left[\frac{3T_{rr}-T_{ii}}{r^3|1-Mr|}\right]_{ret} dV \quad 4.5$$

Here $M_r=\frac{v_i r_i}{c}$ is the Mach number in the direction of the observer, $T_{rr}=T_{ij}r_i r_j$, and $T_{ii}=T_{11}+T_{22}+T_{33}$. Then the spatial derivative is transformed using a time derivative [2]. Physically these equations represent the noise sources. The first line represents the thickness noise the following line represents the loading noise and the third and fourth line represent the quadrupole noise and the thickness noise if the surface is rigid.

Following this the formulation is simplified by neglecting the quadruple term this work is completed by [23]. This also assumes the P' value takes the form of $P'=c^2(\rho-\rho_0)$ the equation can be rewritten then as the times derivatives are inserted inside the integrand obtaining the following equation:

$$4\pi p'(x,t) = \int_{f=0}\left[\frac{\rho_0\left(\dot{U}_n + U_n\right)}{r(1-M_r)^2}\right]_{ret} d_s$$
$$+ \int_{f=0}\left[\frac{\rho_0 U_n((r\dot{M}_r + c(M_r - M^2))}{r^2(1-M_r)^3}\right]_{ret} d_s$$
$$+ \frac{1}{c}\int_{f=0}\left[\frac{\dot{L_r}}{r(1-M_r)^2}\right]_{ret} d_s$$
$$+ \int_{f=0}\left[\frac{L_r - L_M}{r^2(1-M_r)^2}\right]_{ret} d_s + \frac{1}{c}\int_{f=0}\left[\frac{L_r\left(r\dot{M}_r + c(M_r - M^2\right)}{r^2(1-M_r)^3}\right]_{ret} d_s \quad 4.6$$

For this equation M and U are the motion velocity on the surface and the Mach number the distance between the observer and the source are denoted as r, the dot vectors are the time derivatives. This set of equations is used for a moving control surfaces the FWH surfaces used in this project are nonmoving objects and thus the equation needs to be reduced to eliminate these terms. The final equation for FWH formulation determined by [31] and shown by [2] is finally:

$$4\pi p(x,t) = \int_{f=0}\left[\frac{\rho_0 \dot{U}_n}{r}\right]_{ret} d_s + \frac{1}{c}\int_{f=0}\left[\frac{\dot{L_r}}{r}\right]_{ret} d_s + \int_{f=0}\left[\frac{L_r}{r^2}\right]_{ret} d_s \quad 4.7$$

Following this FWH surface are created to extract the data from the isolated propeller. These surfaces have a set of endcaps for the information to pass through as well as an outside surface to capture Far-Field Acoustics. These are shown below.

(a) (b)

Figure 4.17 FWH Surface different Views

(a) (b)

Figure 4.18 Endcaps Different Views

The grid spacing used in the simulation provides a cut off frequency of 5000 Hz this allows for a look into the low-mid frequency cut off range and provides a higher resolution than that of Afari [2] this comes with some serious computational challenges, however. And increases the run time of the simulation by nearly double to collect data for that reason the isolated propellor was ran for 40 iterations then acoustic data was collected for a single final iteration. Below are comparisons of the figures from Afari [2] Figure 4.19 with the current isolated results Figure 4.20 and Figure 4.21.

The pressure distribution across the top and the bottom of the propeller blade must be analyzed as the blade is the main source of noise in this simulation when results of the top and bottom of the blade are compared it can be seen that they are very similar nearly identical which is to be expected. The bottom of the blade has an area of high pressure towards the tips of the blade whereas the same point but below the propeller the pressure is low. This is a physical property of aerodynamics and is fundamental to generating lift in any airfoil. The results for this can be seen in the following figures.

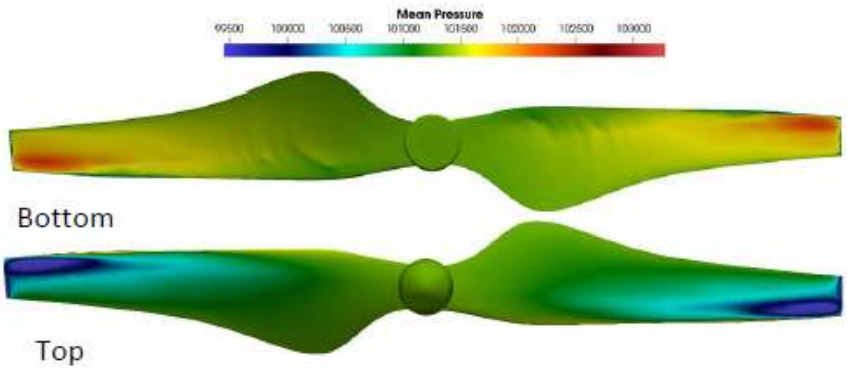

Figure 4.19 Pressure Distribution Across the Rotor Top and Bottom View Afari [2]

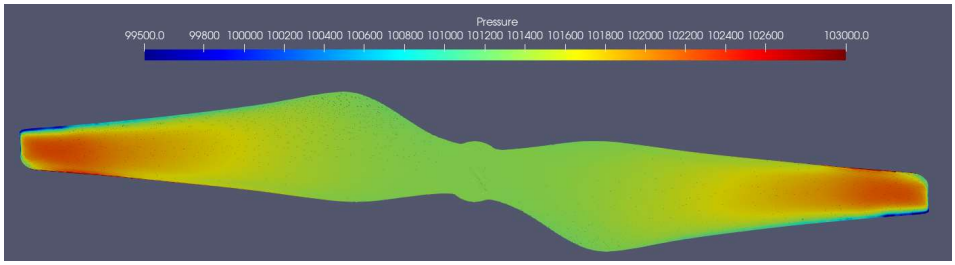

Figure 4.20 Pressure Distribution Across the Rotor Bottom View

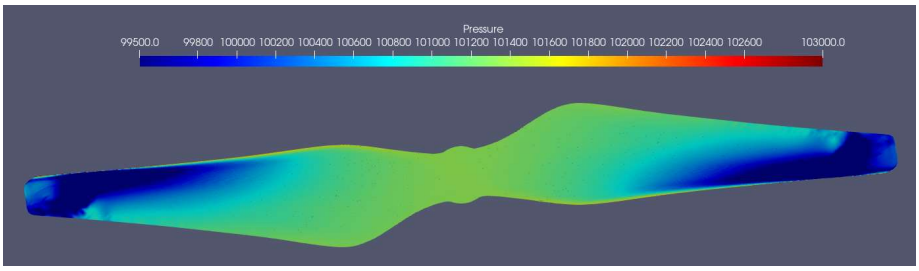

Figure 4.21 Pressure Distribution Across the Rotor Top View

5 Conclusion and Future Work

Each of these individual simulations ran provided adequate data and results to understand what the effects on the thrust distribution the ground can cause. The isolated propeller served as a baseline case and provided a thrust coefficient that is smaller than the rest of the propellers. The partial ground demonstrated the largest of the three thrust variations with the ground effect demonstrating a value in-between each of these variables. This prediction is to be expected. When a craft approaches a ground surface the pressure differential increases between the ground and the prop. Usually this causes an increase in the required power needing to be supplied to the rotor blade to ensure that the same RPM is being used. But in this case due to the RPM being held constant the thrust increases instead. The issue then resides in the partial ground case. The partial ground has a higher thrust coefficient then both the isolated and homogenous cases. This can be due to a variety of reasons but due to a limitation on the research conducted in this area some assumptions must be induced from the figures there is a high amount of curl around the edge of the building. This is most likely causing a large pressure spike in this area which leads to an increase in the thrust coefficient associated with the current results. Further experimentation and understanding would need to be conducted to better understand and analyze these results. The results comparing the isolated propeller to that of the experimental propeller conclude that with a margin of error of only 5 % that

the mesh and therefore the following corresponding meshes may be valid evaluations of the propeller in its cases. The isolated results from Afari [2] compared very well with the results generated by this simulation. The probe data from the partial ground effects and the entire ground effects provided valuable insight into what the acoustic effects of implementing a ground into the simulation and the results of this demonstrated the effects of the ground on the acoustics. Demonstrating safety concerns for both acoustics as well as the aerodynamic concerns of propeller implementation. The implemented check mesh provided valuable insight into the understanding of acoustics but was not needed for performance analysis.

The current scope of this project is to also look at the acoustic data collection from not just probe locations but also from FWH surfaces implemented. This takes a large amount of computational time and has distinct challenges especially with regards to the partial ground effects. The probe data provides valuable data insight and allows sound level to be calculated but the implementation of these surfaces is crucial for further insight. It is also important to note that this is a first step in the overarching scope of the current grant by the NASA ULI project. This is intended to be a “first step” in identifying proper meshing techniques to better understand Urban environments. Eventually a specific rotor blade known as a Joby blade will be used. This blade has a lot more application to actual inner-city travel and will allow for greater understanding of not just numeric trends but also concrete data values. It is important to note that multiple blades as well as eventually a UAV body could be implemented into this simulation albeit with some serious adjustments to the mesh. Included with this currently there are steps being taken toward experimentation being conducted to have valuable experimental data to base future CFD research off. Also, there will be further implementation of gusts to study noise in this mesh space.

6 References

[1] Rizzi, S., Huff, D., Jr, D., Bent, P., Henderson, B., Pascioni, K., Sargent, D., Josephson, D., Marsan, M., He, H., and Snider, R., "Urban Air Mobility Noise: Current Practice, Gaps, and Recommendations," *NASA Technical Paper #2020-5007433*, 2020.

[2] Mankbadi, R. R., Afari, S., and Vladimir, V. G., "High-Fidelity Simulations of Noise Generation in A Propeller-Driven UAV," AIAA Journal, December 29, 2020. https://doi.org/10.2514/1.J059117

[3] Rankine, W., and of Naval Architects, I., On the Mechanical Principles of the Action of Propellers, 1865.

[4] Gutin, L. S., "On the Sound Field of a Rotating Propeller," *NACA TM 1195*, 1948.

[5] Deming, A. F., "Propeller Rotation Noise Due to Torque and Thrust," *The Journal of the Acoustical Society of America*, Vol. 12, No. 1, 2005, pp. 173–182. https://doi.org/10.1121/1.1916089.

[6] Glauert, H., "Aerodynamic Theory," *The Aeronautical Journal*, Vol. 34, No. 233, 1930, p. 409–414.

[7] Gur, O., and Rosen, A., "Comparison between blade-element models of propellers," *The Aeronautical Journal*, Vol. 112, No. 1138, 2008, p. 689–704. https://doi.org/10.1017/S0001924000002669.

[8] Chirico, G., Barakos, G. N., and Bown, N., "Numerical aeroacoustic analysis of propeller designs," *The Aeronautical Journal*, Vol. 122, No. 1248, 2018, p. 283–315. https://doi.org/10.1017/aer.2017.123.

[9] "Four Treatises on Hydrodynamics and Aerodynamics," *International Congress of Mathematicians III*, Vol. 8, No. 1, 1928. https://doi.org/10.1002/zamm.19280080126.

[10] Drela, M., "XFOIL: An Analysis and Design System for Low Reynolds Number Airfoils," 1989. https://doi.org/10.1007/978-3- 642-84010-4_1.

[11] Alvarez, E. J., and Ning, A., "Modeling Multirotor Aerodynamic Interactions Through the Vortex Particle Method," *AIAA Paper 2019-2827 presented at AIAA Aviation 2019 Forum, Dallas, TX*, June 2019. https://doi.org/10.2514/6.2019-2827.

[12] Farassat, F., "Derivation of Formulations 1 and 1A of Farassat," *Langley Research Center Report #20070010579*, 2007.

[13] Lee, H., and Lee, D.-J., "Rotor interactional effects on aerodynamic and noise characteristics of a small multirotor unmanned aerial vehicle," *Physics of Fluids*, Vol. 32, No. 4, 2020, p. 047107. https://doi.org/10.1063/5.0003992.

[14] Mankbadi, R. R., Afari, S. O., and Golubev, V. V., "High-Fidelity Simulations of Noise Generation in a Propeller-Driven Unmanned Aerial Vehicle," *AIAA Journal*, Vol. 59, No. 3, 2021, pp. 1020–1039. https://doi.org/10.2514/1.J059117.

[15] Diaz, P. V., and Yoon, S., "High-Fidelity Computational Aerodynamics of Multi-Rotor Unmanned Aerial Vehicles," *AIAA SciTech*, 2018. https://doi.org/10.2514/6.2018-1266.

[16] Afari, S., and Mankbadi, R. R., "Simulations of Noise Generated by Rotor-Rotor Interactions at Static Conditions," *AIAA Paper 2021-1986 presented at AIAA Scitech 2021 Forum, Virtual Event*, January 2021. https://doi.org/10.2514/6.2021-1986.

[17] Zhou, W., Ning, Z., Li, H., and Hu, H., "An Experimental Investigation on Rotor-to-Rotor Interactions of Small UAV Propellers," *AIAA Paper 2017-3744 presented at 35th AIAA Applied Aerodynamics Conference*, June 2017. https://doi.org/10.2514/6.2017- 3744.

[18] Zhou, T., and Fattah, R., *Tonal Noise Acoustic Interaction Characteristics of Multi-Rotor Vehicles*, June 2017. https://doi.org/10.2514/6.2017-4054.

[19] Lopez, O. D., Escobar, J. A., and Pérez, A. M., "Computational Study of the Wake of a Quadcopter Propeller in Hover," 23rd AIAA Computational Fluid Dynamics Conference, 2017. https://doi.org/10.2514/6.2017-3961.

[20] Mora, R. B., and García, J. C. M., "Helicopter Rotor Ground Effect and Frigate Interaction Investigated by Particle Image Velocimetry," AIAA Journal, Vol. 60, No. 1, January 2022, pp. 129–143. https://doi.org/10.2514/1.J060439.

[21] The OpenFOAM Foundation, "OpenFOAM v9 User Guide,", 2017. URL https://cfd.direct/openfoam/user-guide.

[22] Poinsot, T., and Lelef, S., "Boundary conditions for direct simulations of compressible viscous flows," Journal of Computational Physics, Vol. 101, No. 1, 1992, pp. 104–129. https://doi.org/10.1016/0021-9991(92)90046-2.

[23] Afari, S. O., and Mankbadi, R. R., "Simulations of multi-rotor interaction noise at hovering & forward flight conditions,"

[24] International Journal of Aeroacoustics, Vol. 22, No. 1-2, 2023, pp. 153–187. https://doi.org/10.1177/1475472X231152608.

[25] Deters, R. W., Kleinke, S., and Selig, M. S., "Static Testing of Propulsion Elements for Small Multirotor Unmanned Aerial Vehicles," AIAA Paper 2017-3743 presented at 35th AIAA Applied Aerodynamics Conference, Denver, CO, June 2017. https://doi.org/10.2514/6.2017-3743.

[26] Zawodny, N., Boyd, D. J., and Burley, C., "Acoustic Characterization and Prediction of Representative, Small-Scale Rotary-Wing Unmanned Aircraft System Components," Langley Research Center Report #20160009054, 2016.

[27] Walsh, J. L., Bingham, G. J., & Riley, M. F. (1987). Optimization Methods Applied to the Aerodynamic Design of Helicopter Rotor Blades. Journal of the American Helicopter Society, 32(4), 39–44. https://doi.org/10.4050/JAHS.32.39

[28] Mankbadi, R. R., Hixon, R., Povinelli, L. A., "Very Large Eddy Simulations of Jet Noise," AIAA 2000-2008, 6th AIAA/CEAS Aeroacoustics Conference, Lahaina, Hawaii, 12-14 June 2000.

[29] NASA. (n.d.). Navier-stokes equations. NASA. https://www.grc.nasa.gov/www/k-12/airplane/nseqs.html#:~:text=These%20equations%20describe%20how%20the,France%2C%20in%20the%20early%201800's

[30] Zikanov O. (2010). Essential computational fluid dynamics. Wiley. March 20, 2024

[31] NASA. (n.d.-a). Menter Shear Stress Transport Model. NASA. https://turbmodels.larc.nasa.gov/sst.html

[32] Ffowcs Williams, J.E. and Hawkings, D.L. (1969) Sound Generation by Turbulence and Surfaces in Arbitrary Motion. Philosophical Transactions of the Royal Society A, 264, 321-342.http://dx.doi.org/10.1098/rsta.1969.0031

[33] Measuring levels. Commodious. (n.d.). https://www.commodious.co.uk/knowledge-bank/hazards/noise/measuring-levelsAnalytical Comparison of the Acoustic Analogy and Kirchhoff Formulation for Moving Surfaces Kenneth S. Brentner and F. Farassat AIAA Journal 1998 36:8, 1379-1386

[34] Thai, Austin & Jain, Rohit & Grace, Sheryl. (2019). CFD Validation of Small Quadrotor Performance using CREATE - AV Helios. 10.4050/F-0075-2019-14483.

[35] Russell, C. R., Jung, J., Willink, G., & Glasner, B. (2016). Wind Tunnel and Hover Performance Test Results for Multicopter UAS Vehicles.

[36] Smith, B., Lyrintzis, A., Gandhi, F., and Healy, R., "Evtol rotor noise in ground effect," Proceedings of the Vertical Flight Society 77th Annual Forum, 2021.

[37] Leishman, J. Gordon. (2006). *Principles of helicopter aerodynamics* (Second edition.). Cambridge University Press.

APPENDIX – A

```
clear figure

clear all

%probes

%slave of the living God


z=1; %Change this for different titles of the graphs

varamount=4;%amount of variable lines expected

head=5;%amount of header lines expected

%% soure files

one=("E:\NASA_DOWN\probesforeverything\probes_isolated\0.4\p.dat");

%one=("E:\Final_postProoccsing\Probes\test"); %isolated

two=("E:\Final_postProoccsing\Probes\test1"); %homogeneous case

three=("E:\Final_postProoccsing\Probes\test2"); %non-homogeneous case

%% formatting loop

if z==1

probe=readtable(one,NumHeaderLines=head,ExpectedNumVariables=varamount); %ignore the

warning variable names are set later

elseif z==2

    probe=readtable(two,NumHeaderLines=head,ExpectedNumVariables=varamount);

else

    probe=readtable(three,NumHeaderLines=head,ExpectedNumVariables=varamount);

end

getouttahere=["(",")"];

w=width(probe);
```

```
TF = cellfun(@isnumeric,table2cell(probe(2,:))); % look at the first row of the
table, convert to a cell array temporarily, then create a logical array based on
isnumeric
probenew=num2cell(ones(size(probe)));
for good=1:w
    who=TF(:,good);
    if who==1
        probenew(:,good)=table2cell(probe(:,good));

    else
        probe{:,good}=erase(probe{:,good},getouttahere);
        probenew(:,good)=table2cell(probe(:,good));
        probenew(:,good)=num2cell(str2double(probenew(:,good)));

    end
end

A=cell2table(probenew);
varnames=(["Time","Probe1","Probe2","Probe3"]);
A.Properties.VariableNames=varnames;
%% Plotting
figure('Renderer', 'painters', 'Position', [10 200 880 500])
plot(A.Time,A.Probe1);
xlabel("Time (s)")
ylabel("Pressure (Pa)")
% xlim([.48 .499])
if z==1
title("Probe 1 Pressure (Pa) V.S Time (s) Isolated Propeller")
```

```
elseif z==2
    title("Probe 1 Pressure (Pa) V.S Time (s) Homogenous Ground")
else
    title("Probe 1 Pressure (Pa) V.S Time (s) Non-Homogeneous")
end
%%
figure('Renderer', 'painters', 'Position', [10 200 880 500])
plot(A.Time,A.Probe2)
xlabel("Time (s)")
ylabel("Pressure (Pa)")
if z==1
title("Probe 2 Pressure (Pa) V.S Time Isolated Propeller")
elseif z==2
    title("Probe 2 Pressure (Pa) V.S Time Homogenous Ground")
else
    title("Probe 2 Pressure (Pa) V.S Time Non-Homogeneous Ground")
end
% xlim([.48 .499])


figure('Renderer', 'painters', 'Position', [10 200 880 500])
plot(A.Time,A.Probe3)
xlabel("Time (s)")
ylabel("Pressure (Pa)")
if z==1
title("Probe 3 Pressure (Pa) V.S Time Isolated Propeller")
elseif z==2
    title("Probe 3 Pressure (Pa) V.S Time Homogenous Ground")
else
```

```
    title("Probe 3 Pressure (Pa) V.S Time Non-Homogeneous Ground")
end



%figure of merit calculation for all rotor configurations


clc
clear
%Slave of the living God
Type=1; %this specifies what type you are using 1=isolated 2=Homogeneous 3=non-
homogeneous
isoM=("E:\NASA_DOWN\2.0\postProcessing_0.4\forces\0.3\moment"); %isolated
HomoM="E:\Final_postProoccssing\Probes\test1"; %homogeneous case
nonHomoM="E:\Final_postProoccssing\Probes\test2"; %non-homogeneous case
isoT=("E:\NASA_DOWN\2.0\postProcessing_0.4\forces\0.3\force");
HomoT="E:\Final_postProoccssing\Probes\test1";
nonHomoT="E:\Final_postProoccssing\Probes\test2";
%%
varamount=10;%amount of variable lines expected
head=3;%amount of header lines expected
if Type==1
Momenti=readtable(isoM,NumHeaderLines=head,ExpectedNumVariables=varamount,VariableNam
ingRule=preserve); %ignore the warning variable names are set later
elseif Type ==2
Momenti=readtable(HomoM,NumHeaderLines=head,ExpectedNumVariables=varamount);
else
Momenti=readtable(nonHomoM,NumHeaderLines=head,ExpectedNumVariables=varamount);
end
```

```
% Momenti=Momenti(:,1:10);
getouttahere=["(",")"];
w=width(Momenti);
TF = cellfun(@isnumeric,table2cell(Momenti(2,:))); % look at the first row of the
table, convert to a cell array temporarily, then create a logical array based on
isnumeric
Momentnew=num2cell(ones(size(Momenti)));
for good=1:w
    A=TF(:,good);
    if A==1
        Momentnew(:,good)=table2cell(Momenti(:,good));
        %Momentnew(:,good)=Momenti(:,good);
    else
        Momenti{:,good}=erase(Momenti{:,good},getouttahere);
        Momentnew(:,good)=table2cell(Momenti(:,good));
        Momentnew(:,good)=num2cell(str2double(Momentnew(:,good)));
        %Momenti(:,good)=cell2table(Momenti(:,good));
    end
end
Mi=cell2table(Momentnew);
varnames=(["Time","total_x","total_y","total_z","pressure_x","pressure_y","pressure_z
","viscous_x","viscous_y","viscous_z"]);
Mi.Properties.VariableNames=varnames;
if Type==1
Thrusti=readtable(isoT,NumHeaderLines=head,ExpectedNumVariables=varamount);%ignore
the warning variable names are set later
elseif Type==2
    Thrusti=readtable(HomoT,NumHeaderLines=head,ExpectedNumVariables=varamount);
```

```
else
    Thrusti=readtable(nonHomoT,NumHeaderLines=head,ExpectedNumVariables=varamount);
end


getouttahere=["(",")"];
w=width(Thrusti);
TF = cellfun(@isnumeric,table2cell(Thrusti(2,:))); % look at the first row of the
table, convert to a cell array temporarily, then create a logical array based on
isnumeric
Thrustnew=num2cell(ones(size(Thrusti)));
for good=1:w
    A=TF(:,good);
    if A==1
        Thrustnew(:,good)=table2cell(Thrusti(:,good));


    else
        Thrusti{:,good}=erase(Thrusti{:,good},getouttahere);
        Thrustnew(:,good)=table2cell(Thrusti(:,good));
        Thrustnew(:,good)=num2cell(str2double(Thrustnew(:,good)));


    end
end
%%
Ti=cell2table(Thrustnew);
varnames=(["Time","total_x","total_y","total_z","pressure_x","pressure_y","pressure_z
","viscous_x","viscous_y","viscous_z"]);
Ti.Properties.VariableNames=varnames;
%% Initial conditions
```

```
con=0.1047198;
r=0.24/2; %rotor radius
rho=1.225;%density
A=pi*(r^2); %swept area
omega=(6000*2*pi)/(60); %rotation rate in rad/s
%% Calculations
momenti=mean(sqrt(Mi.total_x.^2+Mi.total_y.^2+Mi.total_z.^2));
thrusti=mean(sqrt(Ti.total_x.^2+Ti.total_y.^2+Ti.total_z.^2));

den=rho*A*omega^2*r^2; %thrust
den1=rho*A*omega^2*r^3;%moment
C_qi=(momenti./den1);
C_ti=(thrusti./den);

T1i=(C_ti.^(3/2));
bi=sqrt(2).*C_qi;
FOM=T1i./bi;

figure (1)
plot(Mi.Time,Mi.total_y);
xlabel('Time (s)');
ylabel('Moment (N-M)');
if Type==1
title('Moment (N-M) V.S Time (s) Isolated Propeller');
elseif Type==2
    title('Moment (N-M) V.S Time (s) Homogeneous Ground')
else
    title('Moment (N-M) V.S Time (s) Non-Homogeneous Ground')
```

```
end



figure (2)
plot(Ti.Time,Ti.total_y);
xlabel('Time (s)');
ylabel('Thrust (N)');
if Type==1
title('Thrust (N) V.S Time (s) Isolated Propeller');
elseif Type==2
    title('Thrust (N) V.S Time (s) Homogeneous Ground')
else
    title('Thrust (N) V.S Time (s) Non-Homogeneous Ground')
end


  %% expiremental
% % %C_t=(0.0097*den);
% % %%NASA Stuff
% % den=rho*A*omega^2*r^2; %thrust
% % diam =9.4/12;
% % rnas=diam/2;
% % Anas=pi*r^2;
% % rhonas =0.023769;
% % %omeganas =6000*con;
% % %denasa=rho*A*(omega*nas)^2;
%  thrustNasa=(4.016/den);


%% uncertainty
```

```
% Isolated
Umi = abs(momenti-max(Mi.total_y));
Uti=abs(thrusti-max(Ti.total_y));
% Display the results
% fprintf('Mean value: %.2f\n', momentp);
% fprintf('Standard deviation: %.2f\n', standard_deviation);
fprintf('Uncertainty Isolated: %.5f\n', Umi);
fprintf('Uncertainty Isolated: %.5f\n', Uti);

% Ground Full
UmG = abs(momentG-max(MG.total_y));
UtG=abs(thrustG-max(TG.total_y));
% Display the results
% fprintf('Mean value: %.2f\n', momentp);
% fprintf('Standard deviation: %.2f\n', standard_deviation);
fprintf('Uncertainty Ground: %.5f\n', Umi);
fprintf('Uncertainty Ground: %.5f\n', Uti);

%Partial Ground
Ump = abs(momentp-max(Mp.total_y));
Utp=abs(thrustp-max(Tp.total_y));
% Display the results
% fprintf('Mean value: %.2f\n', momentp);
% fprintf('Standard deviation: %.2f\n', standard_deviation);
fprintf('Uncertainty Partial: %.5f\n', Ump);
fprintf('Uncertainty Partial: %.5f\n', Utp);
```

```
%% graph FOM
clear figure
y=[76.99 76.54 75.5; 74.19 74.22 74.27 ; 68.08 90.84 71.05;];
X = categorical({'Probe 1','Probe 2','Probe 3'});
X = reordercats(X,{'Probe 1','Probe 2','Probe 3'});
% X = reordercats(X,{'Isolated Rotor','Homogeneous Ground','Partial Ground'});
figure (8)
%bar(X,y,'FaceColor','flat')
% y = [1 3 5; 3 2 7; 3 4 2];
% b = bar(X,y,'FaceColor','flat');
% for k = 1:size(y,2)
%     b(k).CData = k;
% end
% b = bar(X,y,0.3,'FaceColor','flat');
% b.CData(1,:) = [1 0 0];
% b.CData(2,:) = [0 0.5 0];
% b.CData(3,:) = [0 0 0.7];
bar(X,y)
title( 'Sound Pressure Level Comparison')
ylabel ('SPL (dB)')
legend('Isolated Rotor','Full Ground', 'Partial Ground' )
% ylim([3 4]);

% hold on
% bar(2,FOMG)
% hold On
% bar (3,FOMp)
hold off
```

```
%Slave of the living God
clc
clear
q = 0:0.001:2*pi; % angle 0 to 360 degrees in radian
r = 0.1195;          % radius
x = r*cos(q);    % cartesian x coordinate
z = r*sin(q);  % cartesian y coordinate
%% next one is 90
%%
times=linspace(0.44006,0.45,90);
names=0.44:0.00006:0.44996;
% allFiles = dir( 'E:\Final_postProoccssing\polar\90\' );
% allNames = { allFiles.name };
%% draw lines and points
r=0.1195;
 ten=(0:((2*pi)/(length(names))):(2*pi));
x=r*cos(ten);
z=r*sin(ten);
namesn=(ones(1,168));
namesn(1,1:167)=namesn(1,1:167).*names;
comb=([namesn; z./0.1195; -x./0.1195]);
comb=comb';
comb=cell2table(num2cell(comb));
varnames=["Time","X","Z"];
comb.Properties.VariableNames=varnames;

%scatter(x,y);
```

```
%
%  scatter(x,ten)



hold on
for i=1:length(ten)

        line([0 z(i)],[0 x(i)],'lineWidth',5)







end


%% load data do this in  a loop save your data aprop
clear
A=readtable('E:\Final_postProoccsing\polar\so_much\89.csv',VariableNamingRule='preser
ve');
A=renamevars(A,["Points_0","Points_1","Points_2"],["X","Y","Z"]);
% A.("Point ID")=[];
% A.Points_Magnitude=[];
c=max(A.p);
%%
N = 167;
D = 'E:\Final_postProoccsing\polar\so_much';
for k = 0:N
    F = fullfile(D,sprintf('%d.csv',k));
    A = readtable(F,VariableNamingRule='preserve');
```

```
    A=renamevars(A,["Points_0","Points_1","Points_2"],["X","Y","Z"]);
    A.("Point ID")=[];
A.Points_Magnitude=[];
%     A=sortrows(A,3);
%     Y = abs(fft(S.data));
%     F = fullfile(D,sprintf('Y%d.mat',k));
%     save(F,'Y')
% maximum = min(abs(A.Y));
% [x,y]=find(A.X==maximum);
top=[ A.p A.X A.Z A.Y ];
% bottom=[(A.p(1:x-1,:)) A.X(1:x-1,:) A.Z(1:x-1,:) A.Y];
% Z=[(A.p) A.X A.Y A.Z];
% x=width(A);
%
for i=1:length(top)
if k<=83
if top(i,3)<0
top(i,2)=1;
top(i,1)=1;
top(i,3)=1;
top(i,4)=1;

else
top(i,2)=0;
top(i,1)=0;
top(i,3)=0;
top(i,4)=0;
```

```
end

elseif k>83
if top(i,3) >0
top(i,2)=1;
top(i,1)=1;
top(i,3)=1;
top(i,4)=1;

else
top(i,2)=0;
top(i,1)=0;
top(i,3)=0;
top(i,4)=0;

end
end
end
A.p=top(:,1).*A.p;
A.X=top(:,2).*A.X;
A.Y=top(:,4).*A.Y;
A.Z=top(:,3).*A.Z;



c=nonzeros(cell2mat(table2cell(A)));
B=ones(length(c)/4,4);
```

```
 B(:,1)=nonzeros(A.p);
 B(:,2)=nonzeros(A.X);
 B(:,3)=nonzeros(A.Z);
 B(:,4)=nonzeros(A.Y);



scatter3(B(:,2),B(:,3),B(:,4),100,B(:,1),'filled');
ax = gca;
ax.XDir = 'reverse';
%view(-31,14)
xlabel('x')
ylabel('z')
cb = colorbar;
cb.Label.String = 'Pressure';
% plot(t(:,3),t(:,2))
hold on



% scatter(b(:,3),b(:,5),100,b(:,2),'filled');
% ax = gca;
% ax.XDir = 'reverse';
% %view(-31,14)
% xlabel('x')
% ylabel('z')
% cb = colorbar;
% cb.Label.String = 'Pressure';
% hold on
```

```
end
%%


% % Make x-y mesh grid
% % % [xq,yq] = meshgrid(...
% % %   linspace(min(A.X),max(A.X),10959),...
% % %   linspace(min(A.Y),max(A.Y),10959));
% % % % Interpolate using "griddata" function
% % % pq = griddata(A.X,A.Y,A.p,xq,yq,'cubic');
% % % % Visualize the result
% % figure
% % contour(A.X,A.Y,A.p)
% % xlabel('x','FontSize',16)
% % ylabel('y','FontSize',16)
% % c = colorbar;
% % c.Label.String = 'Pressure';
% % c.Label.FontSize = 16;
figure (2)
scatter(A.X,A.Z,40,A.p,'filled')
ax = gca;
ax.XDir = 'reverse';
%view(-31,14)
xlabel('x')
ylabel('y')
cb = colorbar;
cb.Label.String = 'Pressure';
```